The urban dispersion model EPISODE v10.0. Part 1: A Eulerian and sub-grid-scale air quality model and its application in Nordic winter conditions

Paul D. Hamer[1], Sam-Erik Walker[1], Gabriela Sousa-Santos[1], Matthias Vogt[1], Dam Vo-Thanh[1], Susana Lopez-Aparicio[1], Philipp Schneider[1], Martin O.P. Ramacher[2], Matthias Karl[2]

[1]Norwegian Institute for Air Research (NILU), Kjeller, Norway
[2]Chemistry Transport Modelling Department, Institute of Coastal Research, Helmholtz-Zentrum Geesthacht, 21502, Geesthacht, Germany

Correspondence to: paul.hamer@nilu.no

Abstract. This paper describes the Eulerian urban dispersion model EPISODE. EPISODE was developed to address a need for an urban air quality model in support of policy, planning, and air quality management in the Nordic, and, specifically, Norwegian setting. It can be used for the calculation of a variety of airborne pollutant concentrations, but we focus here on the implementation and application of the model for NO_2 pollution. EPISODE consists of a Eulerian 3D grid model with embedded sub-grid dispersion models (e.g., a Gaussian plume model) for dispersion of pollution from line (i.e., roads) and point sources (e.g., chimney stacks). It considers the atmospheric processes advection, diffusion, and a NO_2 photochemistry represented using the photostationary steady state approximation for NO_2. EPISODE calculates hourly air concentrations representative of the grids and at receptor points. The latter allow EPISODE to estimate concentrations representative of the levels experienced by the population and to estimate their exposure. This methodological framework makes it suitable for simulating NO_2 concentrations at fine scale resolution (< 100 m) in Nordic environments. The model can be run in an offline nested mode using output concentrations from a global or regional chemical transport model and forced by meteorology from an external numerical weather prediction model; but it also can be driven by meteorological observations. We give a full description of the overall model function as well as its individual components. We then present a case study for six Norwegian cities whereby we simulate NO_2 pollution for the entire year of 2015. The model is evaluated against in-situ observations for the entire year and for specific episodes of enhanced pollution during winter. We evaluate the model performance using the FAIRMODE DELTA Tool that utilizes traditional statistical metrics, e.g., RMSE, Pearson correlation, R, and bias along with some specialised tests for air quality model evaluation. We find that EPISODE attains the DELTA Tool model quality objective in all of the stations we evaluate against. Further, the other statistical evaluations show adequate model performance, but that the model scores greatly improved correlations during winter and autumn compared to the summer. We attribute this to the use of the photostationary steady state scheme for NO_2, which should perform best in the absence of local ozone photochemical production. Oslo does not comply with the NO_2 annual limit set in the 2008/50/EC directive (AQD). NO_2 pollution episodes with the highest NO_2 concentrations, which lead to the occurrence of exceedances of the AQD hourly limit for NO_2 occur primarily in the winter and autumn in Oslo, so this strongly supports the use of EPISODE in the application of these winter-

time events. Overall, we conclude that the model is suitable for assessment of annual mean NO_2 concentrations and also for the study of hourly NO_2 concentrations in the Nordic winter and autumn environment. Further, in this work we conclude that it is suitable for a range of policy applications specific to NO_2 that include: pollution episode analysis, evaluation of seasonal statistics, policy and planning support, and air quality management. Lastly, we identify a series of model developments

5   specifically designed to address the limitations of the current model assumptions. Part 2 of this two-part paper discusses the "CityChem" extension to EPISODE, which includes a number of implementations such as a more comprehensive photochemical scheme suitable for describing more chemical species and a more diverse range of photochemical environments, and a more advanced treatment of the sub-grid dispersion.

1 Introduction

10   Air pollution represents a major hazard to human health. An estimated 3 million people die each year worldwide due to ambient air pollution (World Health Organization, 2016), which includes combined effects from O_3, NO_2, SO_2, and particulate matter (PM). Of these listed pollutants, PM has the largest impact on mortality and disease burden worldwide. 90% of the world's population breathes air that does not comply with WHO guidelines (World Health Organization, 2016). Further, human exposure to poor air quality is disproportionately weighted to populations living in urban areas where population densities,

15   relatively high levels of pollutant emissions and consequent high background levels of pollutants coincide spatially.

The European Commission Directive 2008/50/EC (EU, 2008) requires that air quality be monitored and assessed via measurement and/or modelling for 13 key pollutants in European cities with populations larger than 250,000 people. Measurements are required in all cases except for when pollutant concentrations are very low. In addition, Directive 2008/50/EC indicates that, where possible, modelling should be applied to allow the wider spatial interpretation of in-situ

20   measurement data. Norway as a European Economic Area (EEA) member adopted these regulations within its own laws.

The health impacts of urban air pollution and the requirements from legislation to provide air quality assessment and management for urban areas combine to create a need to develop urban air quality models. Such models need to provide air quality exposure mapping and to further support policy-making through assessment of emission abatement measures and understanding of the sources, causes and processes that define the air quality.

25   Due to the historical need and priority to assess of transboundary pollution (e.g., Fagerli et al., 2017), finite computational power that limits model resolution, and the resolution of the most commonly used compiled emission inventories, the majority of existing air quality models operate at a regional-scale. See, for example, the regional production of the Copernicus Atmospheric Monitoring System (Marécal et al., 2015) that includes 7 chemical transport models (CTMs) run operationally over a European domain at ~10 km resolution. In another case the CALIOPE system is being run operationally over Spain at

30   ~4 km resolution (Baldasano et al., 2011; Pay et al., 2010) using the Community Multiscale Air Quality Modelling (CMAQ) system, and CMAQ is also being run operationally for the United States at 12 km resolution (Foley et al., 2010). The resolution of regional models means they can provide information at the background scale for urban areas, but this limits them from

2

providing the necessary information for policymakers (e.g., exposure mapping and assessment of abatement measures) at the urban and street scales. This limitation stems from a lack of dispersion at the scale of tens to hundreds of meters that prevents them from simulating the typically higher concentrations found close to pollution sources, which are frequently found in areas of higher population density. In addition, the gridded nature of most emission inventories specifically prevents them from

5   representing the actual geometry of emission sources at the sub-kilometre scale, i.e., line (along roads) and point (e.g., industrial stack emissions) sources. The widely used operational regional air quality models operating on the scale of 4-20 km resolution are therefore unsuitable for studying air quality at the urban and street scales.

Microscale models offer an alternative approach to regional models for simulating pollution dispersion in urban areas at scales relevant for exposure mapping and assessment. Such methods include computational fluid dynamics, large eddy simulations,

10   and Gaussian dispersion modelling. The review of Lateb et al., (2016) and the guidelines of Franke et al. (2011) (including references therein) provide a good overview of the successful application of these methods in this context. In the case of CFD and LES methods, they are typically applied to limited areas in a city and/or for simulations of a short duration due to their computational expense. This therefore limits their application for longer term or wider scale studies of the urban environment. Given the limitations of regional-scale air quality models and microscale models, a need existed to develop the EPISODE

15   urban scale air quality model (Slørdal et al., 2003) with the specific aim of addressing many of their weaknesses. EPISODE is a 3D Eulerian CTM that includes several sub-grid scale processes, i.e., emissions represented as line source and point sources, Gaussian dispersion, and estimation of concentrations at the sub-grid scale in locations specified by the user. EPISODE is typically run at 1×1 km resolution over an entire city with domains of up to ~1000 km^2 in size. These features allow EPISODE to simulate pollutant dispersion at the city scale and the microscales simultaneously. EPISODE's typical model resolution,

20   scale of representation (i.e., down to tens of meters), size of domain (i.e., city scale), the level of detail of its sub-grid scale transport processes (i.e., Gaussian dispersion) and receptor point sampling, place it in the gap between regional-scale air quality models and models able to explicitly capture mean flow and turbulent dispersion due to microscale surface characteristics like urban obstacles.

Other modelling systems have been developed for urban scale air quality modelling motivated by similar needs for urban scale

25   air quality mapping and decision support systems. These include the Danish AirGIS system (Jensen et al., 2001) using the street canyon air quality model OSPM, the CALIOPE-Urban system that couples the CALIOPE regional air quality model with the urban roadway dispersion model R-LINE (Baldasano et al., 2011; Benavides et al., 2019; Pay et al., 2010), the Swedish Enviman system (Tarodo, 2003), and the Austrian Airware system (Fedra and Haurie, 1999). These other models follows different approaches, but they all perform a necessary role in support of air quality management and fill a niche between

30   regional-scale air quality models and the more computationally expensive microscale modelling approaches. Development on EPISODE originally began in the 1980s, which was at a similar point in time to models such as AirGIS outlined in (Jensen et al., 2001) and references therein. Therefore, at the point of its original inception EPISODE was consistent with the state of the art at that time.

The only existing technical description of EPISODE, i.e., Slørdal et al., (2003), describes an older version of EPISODE and is a technical report that has not been peer-reviewed. A strong motivation for this two-paper series is therefore to provide a definitive, up to date, and peer-reviewed record of EPISODE v10.0 and its extensions. This first paper (henceforth part one) of the series, describe the components of EPISODE v10.0, i.e., Eulerian grid processes, photochemistry based on the photo-

5   stationary state (PSS) approximation for NO, NO_2 and O_3 photochemistry, sub-grid processes, and various pre-processing utilities. Importantly, the limitations of the PSS approximation for the NO, NO_2, and O_3 chemical system limit EPISODE's application to conditions where net photochemical production of O_3 makes little contribution to background O_3 levels. Part one, therefore, examines an application of EPISODE in the Nordic winter setting. Part one also briefly outlines the updates in v10.0 relative to the technical description in (Slørdal et al., 2003). The second paper in the series, part two (Karl et al., 2019),

10   describes the EPISODE-CityChem extensions to EPISODE, which includes the implementation of a more comprehensive photochemical scheme that can have wider applicability including lower latitude locations. Part two describes an application of EPISODE-CityChem for the city of Hamburg.

Section 2 of this paper describes the EPISODE model and all of its components including external pre-processing utilities. Section 3 describes the case study and EPISODE model setup for seven cities in Norway. Section 4 describes the results from

15   the case study and provides an evaluation of the model performance. Section 5 contains a summary, and Sect. 6 the future work we have planned to further develop EPISODE independent from the planned work to develop EPISODE CityChem described in part two (Karl et al., 2019).

2 Description of EPISODE v10.0

2.1 Overview of EPISODE v10.0 Model Components

20   The EPISODE v10.0 CTM simulates the emission, photochemistry and transport of NO_x in urban areas with the specific aim of simulating the pollutant NO_2. Figure 1 provides an overview of each of the model components, i.e., model inputs, processes, etc., and how they interact with one another.

The Eulerian 3D grid model is described in Sect. 2.2.1 and consists of an advection scheme, vertical and horizontal diffusion schemes, and area gridded emissions. The Eulerian grid model also includes the treatment of the initial and boundary conditions

25   from background concentrations of pollutants, and the photo-stationary state scheme for NO_2, NO, and O_3 chemistry. We also discuss the topography inputs and the surface roughness inputs there.

The sub-grid model components in EPISODE are described in Sect. 2.2.2. They consist of line and point source sub-grid emissions and Gaussian dispersion of both source types. The last component of the sub-grid model consists of a concentration sampling methodology of the Gaussian dispersion at user specified receptor points. As a result, EPISODE provides output

30   concentrations in the 3D grid and at the receptor points. The user defines the location of the receptor points and practically EPISODE can be run with up to 35,000 receptor points distributed over a city before significant degradation in computational performance occurs with higher numbers of points. The user can freely either define a regular grid at a fine scale, align the

receptor points near pollution sources, e.g., along road routes, or to enact some combination of both strategies. Note that the solution to the PSS for NO_2, NO, and O_3 is also calculated at each receptor point.

The emissions inputs can be setup in a fully customisable manner such that emissions from a single sector or sub-sector can be emitted as either area gridded or sub-grid emissions, or as both. In practice, the choice to emit a pollutant as area gridded or sub-grid emissions depends on the specific application of the EPISODE model, and the level of detail that exists on the spatial distribution for a particular emission sector.

EPISODE is driven by different meteorological inputs in the Eulerian 3D grid (described in Sect. 2.3). In addition, external pre-processing utilities are used to prepare some of the meteorological inputs as well as other inputs into specific formats (e.g., emissions and boundary conditions) required by EPISODE (see Sect. 2.4).

EPISODE v10.0 advances beyond the EPISODE version described in (Slørdal et al., 2003) in the following ways:

- Adaptation to run with meteorological input from NWP models.
- Adaptation to handle netcdf I/O.
- Adaptation to run with background chemical forcing from a regional AQ model.
- Simplification of the line source/receptor point dispersion that removes the possibility of double counting errors and saves computation time.
- Adaptation to be a standalone model separate from the AirQUIS air quality management system (Endregard, 2002; Sivertsen and Bøhler, 2000; Slørdal et al., 2008b, 2008a).
- Calculation of the PSS every dynamical timestep instead of every hour and throughout the entire vertical extent of the model instead of only at the surface.
- Addition of a new treatment of vertical eddy diffusivity specialised for urban conditions.

EPISODE can also simulate the emission and transport of both PM2.5 and PM10 using all of the modelling components relevant for NO_2 except the PSS. Currently, both PM2.5 and PM10 are treated as inert tracers with just a single size bin with no secondary aerosol formation, but this will be modified in future versions of the model (see Sect. 6 and part two/ Karl et al., 2019 for further explanation). In addition, this future work will be supported by recent developments in PM emission process modelling (Denby et al., 2013; Grythe et al., 2019).

2.2 Description of Individual Model Components

2.2.1 Eulerian Grid Model

The model horizontal gridding is specified in Universal Transverse Mercator (UTM) coordinates. The horizontal resolution has ranged between 200 m × 200 m to 1 km × 1 km in all recent applications of the model, but 1 km × 1 km is the resolution most typically used. The vertical grid is a terrain-following sigma coordinate system defined from an idealised hydrostatic pressure-distribution. EPISODE is typically run with a relatively high vertical resolution for a CTM with a surface layer thickness of only between 19 and 24 meters in height. This helps EPISODE to represent higher concentrations in the surface

layer. We usually include between 6 to 14 vertical layers within the lowest 500 m of the atmosphere, between 3 to 11 vertical layers between 500 m and 1.5 km of the atmosphere and between 4 to 11 vertical layers above 1.5 km in the free troposphere up to the typical vertical limit at 4000 m. Note that this upper limit is not a hard limit. The topography within the domain is defined on the Eulerian horizontal grid in terms of the average elevation above sea level in meters. It is specified as an input

5   file to the model in ASCII format either according to mapping information or as a constant across the domain.

The horizontal resolution of the Eulerian gridding in EPISODE has constraints applied on it arising from the equations governing the transport. The terms describing the vertical turbulent diffusion are represented according to the mixing length theory (Monin-Obukhov similarity theory). Monin-Obukhov similarity theory is only applicable as long as the chemical reaction processes are slow compared to the speed of the turbulent transport. This condition is not satisfied only in cases with

10   extremely fast chemical systems, e.g., oxidation of monoterpenes above forest canopies. The O_3 and NO_x chemical system is sufficiently slow for this condition to be satisfied. In addition, the characteristic time and length scales for changes in the mean concentration field must be large compared with the scales for turbulent transport (Seinfeld and Pandis, 2006), e.g., the scale at which large eddies are resolved. The validity of Monin-Obukhov similarity theory at small spatial scales places a limit on the resolution of the Eulerian main grid in EPISODE. In our applications here, we use a horizontal resolution of 1×1 km,

15   which should be well above the limitation created by these issues.

The pollutant concentrations are calculated by integrating forward in time the solutions for the 3D advection, diffusion, and photochemistry equations using operator splitting to separately solve the processes. The transport of pollutants in and out of the model domain is implicitly considered within the 3D advection equations. The derivation of the sigma-coordinate transform of the advection/-diffusion equation is described in the technical report (Slørdal et al., 2003).

20   EPISODE's numerical time step is calculated dynamically based on the critical time steps associated with the solution of the 3D advection and diffusion processes. The shortest critical time step across the three processes is then selected and applied for each process, including the PSS chemistry for NO_2, NO, and O_3 at the grid-scale. The time step is rounded downward to ensure that nsteps = 3600(s)/dt is always an integer value. This way, all operations are performed an even number of times so that every second operator sequence is a mirror in time of the first sequence to reduce time-splitting errors. The dynamical timestep

25   typically has a duration of a few minutes.

Different schemes have been developed for the 3D advection and diffusion transport processes (see Table 1), and for other processes on the 3D grid, e.g., the treatment of background pollutant concentrations (see Table 2). These different schemes are described below.

3D Advection Schemes

30   Advection is used in EPISODE to represent both bulk transport both in the horizontal and the vertical. In the vertical dimension the advection term encompasses bulk vertical transport arising from convection that is assumed to be represented at the grid-scale in the input wind fields. For example, in the case where EPISODE uses 1×1 km meteorological input (see Sect. 3 case study) from the Applications of Research to Operations at Mesoscale (AROME) (Bengtsson et al., 2017) NWP model, deep

6

convection is explicitly resolved (Seity et al., 2011) at this resolution while shallow convection is represented by a parameterization (Pergaud et al., 2009).

Two different horizontal advection schemes are implemented in EPISODE and a single scheme for vertical advection scheme. The first advection scheme is an implementation of (Bott, 1989, 1992, 1993) consisting of a 4th-order positive definite scheme.
The scheme calculates fluxes between the grid cells based on a local area-preserving 4th-degree polynomial describing the concentration fluctuations locally. The Bott scheme (1989, 1992, 1993) has good numerical properties and small numerical diffusion, i.e., $< 1\%$ in the most extreme cases (refer to Fig. 1f in Bott, 1989). Artificial numerical diffusion is expected to arise in any Eulerian scheme, e.g., close to large pollution sources. It employs a time splitting method to solve advection separately in the x and y directions with the order of operations for the x and y-axes alternating every second timestep. This scheme is used in every current application of the EPISODE model.

The second advection scheme is a variation of the first Bott scheme and consists of a 4th-order positive definite and monotone scheme. This implementation of the Bott scheme has only been used experimentally in EPISODE.

EPISODE has various methods for specifying the boundary conditions for background concentrations (see Sect. 2.2.1). For each method after the first time step (in which case background concentrations are set as the initial concentrations in all the model domain), the background concentrations are specified in grid cells bordering the model domain (with the same horizontal and vertical resolution) in the x, y, and z dimensions at every time step. The background concentrations in these grid cells are included in the solution for the advection, and by this mechanism background concentrations are transported into the domain. Imposing a background concentration in the boundary grid cells can result in spurious wave reflections at the inflow/outflow boundary. This problem is addressed via a modification of Bott's scheme for advection near the boundaries. A 1st order polynomial is used in the model grid cells bordering the model domain boundary, i.e., [1, y], [X,y], [x, 1], or [x,Y] (X and Y represent the last grid cells in the x and y dimension), to compute the fluxes in and out of the model domain across the boundary. A 2nd order polynomial is used in the second cells of the model domain from the boundary, i.e., [2, y], [X-1, y], [x, 2], or [x, Y-1]. The Bott scheme 4th-order polynomial is used in the third cells of the model domain from the boundary, i.e., [3, y], [X-2, y], [x, 3], or [x, Y-2] and the other cells of the inner model domain. As a test of the model's treatment of boundary conditions, the entrainment of ozone and $PM_{2.5}$ from the boundaries into the inner domain was studied in an artificial simulation in Appendix D of part two of this article (Karl et al., 2019).

Vertical advection is calculated using the simple upstream method, which has the property of being strongly diffusive. However, this numerical diffusion is insignificant in comparison to the magnitude of the vertical turbulent diffusion term. The upstream method implicitly assumes that the three-dimensional wind field is free of divergence and that it therefore attributes vertical motion to either convergence or divergence in the input horizontal wind fields. This ensures that the upstream method maintains mass conservation. This assumption should be satisfied within the wind fields from an NWP model, for example.

Vertical and Horizontal Diffusion Schemes

The values of the eddy diffusivities depend on the properties of the flow field, which is difficult to solve in the grid resolution used here. Therefore, both the horizontal and vertical eddy diffusivities are calculated on the Eulerian grid using parameterisations. The transport of pollutants in the vertical direction is often dominated by turbulent diffusion. The parameterisation of the vertical eddy diffusivity, therefore, has important consequences for the vertical profiles of pollutant concentrations.

In the case of horizontal diffusion, a single parameterisation scheme has been implemented that consists of the fully explicit forward Euler scheme (Smith, 1985).

In EPISODE, the model user can choose between two different parameterisations of the vertical variations of vertical eddy diffusivity, $K^{(z)}$: (1) the standard $K^{(z)}$ method, which is the default used in every current application of EPISODE; and (2) the new urban K(z) method, which has been newly implemented in the EPISODE model. These are both described below. Both parameterizations depend on the atmospheric stability of the Planetary Boundary Layer (PBL) and the vertical wind shear. The stability regime (related to atmospheric buoyancy in the PBL) affecting these $K^{(z)}$ methods is defined with a non-dimensional number z/L, where z is the height above the ground and L is the Monin-Obukhov length. The vertical wind shear is defined by the friction velocity, u_* (ms^{-1}). Both L and u_* are estimated from the input meteorological variables on the 3D Eulerian grid; please refer to Sect. 2.2.2 in part two of this paper (Karl et al., 2019) for further details. Note that the surface roughness is also required for the computation of u_*. In accordance with Monin-Obukhov similarity theory, it is assumed that chemical species have non-dimensional profile characteristics similar to potential temperature, θ, such that $K^{(z)}$ equals the eddy diffusivity of the heat flux. In order to model the turbulent processes in the PBL in a realistic manner, it is essential to consider the vertical variation of the exchange coefficients. In the explicit closure schemes used here, profiles of $K^{(z)}$ are reconstructed from L and u* to account for the vertical variation of the turbulent exchange coefficients.

The applied vertical eddy diffusivity, $K^{(z)}$, is defined as a sum of two terms:

$$K^{(z)} = K_*^{(z)} + K_0^{(z)}, \qquad (1)$$

where $K_*^{(z)}$ is a parameterisation depending on stability regime and $K_0^{(z)}$ is an added background diffusivity term. $K_0^{(z)}$ is only applied within the boundary layer.

The standard $K^{(z)}$-method is based upon the description given in Byun et al. (1999) and included in Sect. S1 of the Supplement. The standard $K^{(z)}$-method uses a constant background diffusivity of $K_0^{(z)} = 0.01$ m^2 s^{-1}.

We now describe the new urban $K^{(z)}$ method here in the main text. For neutral conditions the expression from Shir (1973) is adopted:

$$K^{(z)} = \kappa u_* z \exp\left(\frac{8fz}{u_*}\right), \qquad (2)$$

where κ = 0.41 is the Von Kármán constant, and f is the Coriolis parameter.

For unstable conditions, we use the complex polynomial expression by Lamb and Durran (1978), which is applied as a component within a more comprehensive scheme in McRae et al. (1982).

For stable conditions, a modified equation by Businger and Arya (1974) is used. Businger and Arya (1974) developed a steady state, first-order numerical $K^{(z)}$-model based on a non-dimensional eddy viscosity derived from the empirical log-linear profile for the stable atmospheric surface layer. In this equation, the temperature gradient parameterisation from Businger et al. (1971) is replaced by the non-dimensional temperature gradient (Φ_H) given by Beljaars and Holtslag (1991):

$$\Phi_H = 1 + \frac{z}{L}\left[\alpha\sqrt{1 + \frac{2}{3}\frac{\alpha z}{L}} + \beta e^{-\delta\frac{z}{L}}\left(1 + \gamma - \delta\frac{z}{L}\right)\right], \qquad \textbf{(3)}$$

where the suggested values of the empirical coefficients are: $\alpha = 1$, $\beta = 2/3$, $\gamma = 5$, and $\delta = 0.35$. The expression of Businger and Arya (1974) for the vertical eddy diffusivity under stable conditions consequently becomes:

$$K_*^{(z)} = \frac{\kappa u_* z}{0.8\left(1 + \frac{z}{L}\left[\alpha\sqrt{1 + \frac{2\alpha z}{3L}} + \beta e^{-\delta\frac{z}{L}}\left(1 + \gamma - \delta\frac{z}{L}\right)\right]\right)} exp\left(\frac{8fz}{u_*}\right). \qquad \textbf{(4)}$$

Note that the expression from Beljaars and Holtslag (1991) is scaled by 0.8 to be in better agreement with the temperature gradient from LES computations of the stable boundary layer made by Basu and Porté-Agel (2006).

The new urban $K^{(z)}$-method, considers a baseline turbulent mixing due to the urban roughness and anthropogenic heating effect in cities, with an apparent eddy diffusivity of (Slørdal et al., 2003):

$$K_*^{(0)} = \begin{cases} (2\,\Delta z_1)^2/3600s & \text{for } u_* > 0.2 \text{ ms}^{-1} \\ (\Delta z_1)^2/3600\ s & \text{for } u_* > 0.1 \text{ ms}^{-1} \end{cases}, \qquad \textbf{(5)}$$

with a linear variation of $K_0^{(z)}$ between the two u_* limits.

The particular choice of $K_0^{(z)}$ is based on a scale analysis. This analysis assumes that the respective minimum values of $K^{(z)}$ should be large enough to mix an air-column with a thickness of Δz_1 or $2\,\Delta z_1$ during a one hour period (thickness of the surface layer, i.e., the lower-most model layer), when u_* is less than 0.1 ms^{-1} or larger than 0.2 ms^{-1}, respectively (Slørdal et al., 2003). For u_* less than 0.1 ms^{-1} and $\Delta z1 = 20$ m, $K_0^{(z)}$ becomes equal to 0.11 m^2 s^{-1}. For u_* greater than 0.2 ms^{-1} and $\Delta z1 = 20$ m, $K_0^{(z)}$ becomes equal to 0.44 m^2 s^{-1}.

The dimensionless parameter, surface roughness, z0, is required by the vertical diffusion schemes to help calculate the extent of the vertical turbulent mixing. Surface roughness has to be specified on the Eulerian grid within an ASCII input file. Surface roughness can either be specified as a constant across the whole domain, it can be specified according to an external map of the land cover type across the domain, or the surface roughness can be imported from the NWP into EPISODE.

Area Gridded Emissions

Emissions in EPISODE can be input directly into the 3D Eulerian grid as area source emissions. In this case, emission inputs have to be specified on the domain grid at the working resolution of the model for every hour of the simulation EPISODE also

supports full customisability for the injection heights allowing any proportion of the emission to be emitted at a particular layer. Further details on the area emissions and the input files are described in Appendix A.

EPISODE is typically run using either top-down or bottom-up emissions that undergo pre-processing to set the temporal variability (hourly, daily, and weekly) in the emissions to any desired temporal variability.

5 Boundary and Initial Conditions from the Pollutant Background Concentrations

Three options exist (see Table 2) for the specification of pollutant initial and boundary conditions in EPISODE. The first option is to specify a single background concentration at all locations both in the model domain (for initial conditions) and in the grid cells adjoining the model domain. In this case, concentrations can be specified to be time-varying on an hourly basis (only recommended in specific instances), or to remain constant in time (only recommended for testing purposes). This option could

10 be used in a situation when only a single background observation station existed near a city in order to create a time series for a pollutant. The time-varying background concentration is specified in an ASCII input file while the time-invariant concentration is specified in the EPISODE run file.

The second option is to specify a single vertical profile of background concentrations for every grid cell in the horizontal domain and adjoining background grid cells. The vertical profile must have a vertical resolution matching the model's

15 configuration. This can be done so that the profile is defined on an hourly basis or remains constant in time. The latter option is only recommended for testing purposes, but the time-varying option would be appropriate if the background concentrations are defined by a coarse horizontal resolution (i.e., > 50 km) regional or global CTM. If used, the temporally varying vertical profiles and the constant vertical profile need to be specified in ASCII input files that are referenced in the EPISODE run file. The last option allows specification of background concentrations on the 3D-grid of the model. In this case, the concentrations

20 are specified on the same horizontal and vertical grid as the model and the adjoining grid cells outside of the model domain in the x, y, and z dimensions. The background concentrations are specified on an hourly basis in NetCDF or ASCII input files. This option in EPISODE gives the opportunity to run EPISODE in a one-way nesting configuration embedded within a regional-scale CTM. So far, this option has been used with three different regional-scale CTMs to provide the fields of pollutant background concentrations. In the first example, outputs from the Copernicus Atmospheric Monitoring Services (CAMS)

25 regional production (Marécal et al. 2015) were interpolated from their 10 km horizontal resolution down to a resolution of 1 km. This configuration has been used in the Nasjonal Beregningsverktøy (NBV) (Tarrasón et al., 2017) and BedreByLuft projects (Denby et al., 2017), which both focused on air quality in Norwegian cities. In the second example, output from the EMEP CTM model (Simpson et al., 2012) has also been used in similar fashion to provide background concentrations. In the third example, the CMAQ model (Byun and Schere, 2006) was used to provide the background concentrations where the

30 CMAQ output was interpolated from 4 km horizontal resolution down to ~1 km. CMAQ has been used in the example presented in part two of this article (Karl et al., 2019).

Photo-stationary State Scheme

EPISODE has been designed to be used in urban environments at high latitudes. Under conditions that are polluted (in terms of NO_x) and that have relatively low levels of sunlight, it is possible to make simplifying assumptions about the photochemistry governing the pollutant NO_2.

5 Only a small fraction of NO_x emitted from motor vehicles and combustion sources is in the form of NO_2 (e.g., with an approximate mean of 15%), the largest fraction being NO. The majority of ambient NO_2 originates from the subsequent chemical oxidation of NO. Under polluted, low-light conditions, the vast majority of this oxidation occurs via reaction with O_3 (R1).

$$NO + O_3 \rightarrow NO_2 + O_2 \quad \text{(R1)}$$

10 NO_2 readily undergoes photolysis via (R2).

$$NO_2 + h\nu \rightarrow NO + O(^3P) \quad \text{(R2)}$$

Even at the latitude of Oslo, NO_2 can have a lifetime with respect to photolysis on the order of minutes at midday in winter. The reaction R2 and the subsequent reformation of O_3 via (R3) must therefore be considered if we want to describe NO_2 concentrations under these conditions.

15
$$O(^3P) + O_2 \rightarrow O_3 \quad \text{(R3)}$$

Reaction (R3) between the oxygen radical ($O(^3P)$) and molecular oxygen (O_2) occurs very rapidly and can be assumed to occur instantaneously. We can then reduce the photochemical system describing NO_2, NO, and O_3 to the equilibrium reaction described in equation R4.

$$NO_2 + h\nu \leftrightarrow NO + O_3 \quad \text{(R4)}$$

20 Whereby the forward reaction describes the production of NO_2 via the reaction (R1) (reaction coefficient $k_{(O3 + NO)}$), and the backward reaction (rate coefficient described by $J$$NO_2$) consists of the combined photo-dissociation of NO_2 (via (R2)) and the subsequent, assumed, instantaneous formation of O_3 (via (R3)). The reaction rate for (R2) is calculated using a parameterisation (Simpson et al., 1993) that uses sun angle and cloud cover to calculate $J$$NO_2$, which is described by Eq. S2.2b within the S2 supplement. We assume that this photochemical mechanism is adequate for polluted Nordic wintertime conditions when net

25 photochemical production of O_3 and losses of NO_x via nitric acid production are at a minimum. However, when the solar ultraviolet (UV) radiation is stronger, in particular during summer months or at more southerly locations, net ozone formation may take place in urban areas at a certain distance from the main emission sources (Baklanov et al., 2007). Please refer to part two of this article (Karl et al., 2019) where the EPISODE-CityChem model is described, which uses a more comprehensive photochemical scheme suitable for more sunlit environments.

30 The PSS approximation is used to resolve the NO_2, NO, and O_3 photochemistry on the 3D Eulerian grid and at the receptor points for the sub-grid scale model. The PSS is an analytical mathematical solution that can be applied to R4 to estimate the concentrations of NO_2, NO, and O_3. The PSS has two key assumptions. First, the chemical system is in equilibrium, and, second, that equilibrium is attained instantaneously. These assumptions imply that the residence time of pollutants is much

larger than the chemical reaction time scale, and they are valid for polluted urban conditions. Section 2 in the Supplement gives an in-depth explanation of the PSS and how it is applied in this case for R4.

Taken together, the PSS and its application to R4 is therefore adequate for the Nordic case studies we present in this paper and for the previous and existing applications of the EPISODE model in Norway.

2.2.2 Sub-Grid Scale Model Components

Line and Point Source Emissions

We describe here the implementation of the sub-grid scale emissions in EPISODE. The line source and point source emissions are prepared in advance by one of two possible pre-processing utilities. These utilities are described in Sect. 2.4.

For the line sources, these tools prepare two emission files that are defined in the runfile and read directly into EPISODE at run time. The files describe necessary details such as location, road length and emission source strength. Further details of both files are described in Appendix A. The point source emissions are used for describing emissions from stacks. The details of each stack are specified in a separate emission file that detail the emission source, e.g., stack height and emission rate. Further details are described in Appendix A. EPISODE reads in this information at runtime and calculates the injection heights for the point source emission using a parameterisation based on (Briggs, 1969, 1971, 1974, 1975) that considers the processes of stack downwash, and buoyancy-driven plume rise under different stability conditions.

The stack downwash process modifies the physical height of the chimney to estimate an effective stack height (Briggs, 1974). Buoyancy-driven plume rise will affect the final plume height in different ways according to the boundary layer stability conditions, and therefore there are different parameterisations for either unstable and neutral conditions or stable conditions. The final injection height is calculated by taking into account the effects of the adjacent building (considering its height and width) on building-induced disturbances of the plume flow, plume penetration through elevated stable layers, and topography. Further details of the parameterisations are described in S3 of the supplement.

Line Source Gaussian Dispersion

The line source model is based upon the steady-state integrated Gaussian plume model HIWAY-2 (Petersen, 1980). A fixed rectangular area of influence surrounds each road link that defines the zone within which emissions from line sources are assumed to affect concentrations at receptor points within a single dynamical timestep. Figure 2 shows an illustration of the area of influence around an example road link. The boundaries of the distance of influence extend R_{inf} (the influence distance) from the road link centres perpendicular to the road link direction. In the longitudinal direction, the distance of influence extends R_{inf} from the two ends of each road link. The area of influence excludes receptor points assumed to be on the road links themselves, which is defined by the distance R_{min} (Fig. 2). R_{min} is 5 meters plus half the road link width.

HIWAY-2 resolves the dispersion from the line sources by splitting each road link up into smaller line source segments and then calculating the dispersion from these segments individually. The line source segments are of equal length and are spaced equally along the road links. The emission intensities from each segment, E_l, are calculated as a fraction of the total emission along the road link, E_R, according to

12

$$E_l = E_R \times \frac{D_l}{D_R} \quad (6)$$

where D_l is the length of the line source segment and D_R is the total length of the road link. Therefore, all of the segments emit equal pollutant mass, which is proportional to the fractional length of the road segment D_l/D_R. Note that E_l has units of gs⁻¹ whereas E_R has units of gs⁻¹.m.

5   HIWAY-2 only calculates the dispersion from the line sources to each of the receptor points within their respective areas of influence during the last dynamical timestep of each hour. Note that EPISODE only outputs pollutant concentrations on an hourly basis. Prior to the last dynamical timestep, line source emissions are only emitted directly into the Eulerian grid (see the relevant section further in Sect. 2.2.2). The implicit assumption is that due to the short transport distance, emissions from road links can only affect receptor point concentrations within the distance of influence, R_{inf}, on short timescales equivalent to

10   a single dynamical timestep. The length of the dynamical timestep scales with the wind-speed such that higher wind speeds result in shorter dynamical timesteps. The user can set the R_{inf} for each road link, but typically a value of 300 m is used. That is the R_{inf} used in the case study in this paper, which corresponds to a value well below the simulated distance typically travelled by an airmass in a single dynamical timestep.

The line source dispersion model is described in further detail in S4 of the supplement.

15   **Point Source Gaussian Dispersion**

Two point source plume parameterisations have been implemented in EPISODE to represent dispersion from chimney stacks. The first scheme is a Gaussian segmented plume model called SEGPLU (Walker and Grønskei, 1992) following the general method described by (Irwin, 1983). The second scheme is a puff model called INPUFF (Petersen and Lavdas, 1986). Both schemes use point source emissions and their injection heights calculated following Briggs (1969, 1971, 1974) described

20   earlier in Sect. 2.2.2 and S3 of the supplement. The emissions from point sources are treated as a sequence of instantaneous releases of a specified pollutant mass that each then, in turn, becomes a discrete puff or plume segment. The subsequent position, size and concentration of each plume segment/puff is then calculated in time by the model during each dynamical timestep. This information is used to calculate a plume segment/puff's contribution to the receptor point surface concentrations during the last dynamical timestep of each hour.

25   Plume segments and puffs stop being traced during any dynamical timestep in the following cases: (1) they move outside of the model domain; (2) they become too large; (3) they encounter a large change in wind direction causing them to become spatially separated. If the segments or puffs become too large or are separated whilst within the model domain, the pollutant mass within them is transferred to the grids in which they currently reside during that dynamical timestep, else they are deleted (see further in Sect. 2.2.2 for more details).

30   The SEGPLU and INPUFF models are described in further detail in S5 and S6 of the Supplement, respectively.

Receptor Point Concentration Calculation

The concentrations at receptor points are calculated at the end of each hour by combining the concentrations at the surface layer of the Eulerian grid with the contributions from line and point sources. Up until that timestep, the model only calculates

the chemistry and transport on the Eulerian grid, while also simultaneously calculating the position and concentration of plume segments/puffs. The receptor point concentration at the end of each hour can be described by equation (7),

$$C_{rec}^t(r^*) = C_m^{t-1} + \sum_{l=1}^{L} C_{line,l}^t + \sum_{p=1}^{P} C_{point,p}^t \quad (7)$$

where $C_{rec}^t(r^*)$ is the receptor point concentration at receptor point r^*, at time t, C_m^{t-1} is the Eulerian grid concentration from

5   the penultimate dynamical timestep during each hour (for the grid cell x,y,z=1 where r^* is located), $C_{line,l}^t$ is the line source segment concentration contribution from line source segment l, and $C_{point,p}^t$ is the point source concentration contribution from a plume segment/puff, p. To resolve equation (7), EPISODE sums up the concentration contributions from the total number of line source segments, L, within R$_{inf}$ distance of the receptor point, and the total number of point sources P. The Eulerian grid concentration from the penultimate dynamical timestep, C_m^{t-1}, is used to prevent double counting because it does not include

10   line and point source emission contributions from the final, and current, dynamical timestep in the hour. Testing (not shown) demonstrates that using this assumption in combination with an R$_{inf}$ of 300 m (see earlier in Sect. 2.2.2) reliably reduces double counting of emissions to negligible levels.

For the simulation of NO$_2$, EPISODE resolves Eq. (7) for both NO and NO$_2$, thus calculating $C_{rec}^t(r^*)$ for both compounds. Using the Eulerian grid concentration of ozone combined with the NO and NO$_2$ receptor point concentrations, the

15   photochemistry is solved at each receptor point using the PSS to create updated concentrations for NO$_2$, NO, and ozone that are provided as the hourly model outputs.

Interaction Between Receptor and Eulerian Grid Concentrations

Until the final dynamical timestep of the hour, the emissions from line source segments are emitted directly into the grid in which they reside during each timestep. Each line source segment in a Eulerian grid cell (x,y,z) makes a contribution to the

20   Eulerian grid concentration, C_m, which can be described as a tendency, $dC_{m,L^*}/dt$, via

$$\frac{dC_{m,L^*}}{dt} = \sum_{l^*}^{L^*} \frac{E_{l^*}}{V_{(x,y,z)}} \quad (8)$$

where $V(x,y,z)$ is the volume of Eulerian grid cell (x,y,z) into which the emissions occur, and dt is the length of the dynamical timestep. Since we are discussing line segments within a specific grid cell we use a specific and distinct notation different from that in Eq. (7). Therefore, a line source segment in a particular grid cell (x,y,z) is denoted as, l^*, and the total number of line

25   segments in a grid cell as L^*. In practice, the emissions from road links are emitted directly into the lowest layer of the Eulerian grid. Line segments are sufficiently short in length that it can be considered that each one can emit entirely within a single Eulerian grid cell.

The change in grid concentration, $\Delta C_{m,L^*}$, due to line source segment contributions is calculated via

$$\Delta C_{m,L^*} = \frac{dC_{m,L^*}}{dt} \times dt \quad (9)$$

30   In the last dynamical timestep of the hour, pollutants from line sources are both emitted directly into the Eulerian grid according to (8) and are also dispersed to the receptor points according to descriptions earlier in Sect. 2.2.2 and S4 of the supplement.

14

Point source emissions also contribute to both the concentrations at receptor points and the Eulerian grid. Point sources continually emit plume segments or puffs every dynamical timestep that are dispersed and advected according to Sect 2.2.2 above, and S5 and S6 of the supplement. At the end of each hour, plume segments/puffs are assessed to see if they co-locate with receptor points at the surface, and in this case, they contribute to the receptor point concentrations via Eq. (7). In the case that plume segments/puffs become invalid, they will be deleted, and the pollutant mass within them, m_p, will be added to the concentration of the grid cell in which they reside as a tendency specific to that plume segment/puff, $dC_{m,p}/dt$. This tendency is calculated via

$$\frac{dC_{m,p}}{dt} = \frac{m_p}{V(x,y,z) \times dt} \quad (10)$$

and the change in grid concentration, $\Delta C_{m,p}$, resulting from the deleted plume segment/puff mass is calculated via

$$\Delta C_{m,p} = \frac{dC_{m,p}}{dt} \times dt \quad (11)$$

2.3 Meteorological Inputs

The meteorological inputs can either be provided by a separate NWP, from The Air Pollution Model (TAPM), or from an observationally driven diagnostic model called MCWIND. These different meteorological inputs drive the transport processes at both the grid and sub-grid scales.

The Applications of Research to Operations at Mesoscale (AROME) (Bengtsson et al., 2017) and Weather Research and Forecasting (WRF) (Skamarock et al., 2019) NWP models have both been used to provide inputs for EPISODE. In the case of AROME, we access the Norwegian Meteorological Institute's THREDDS server (https://thredds.met.no/thredds/catalog.html, last access: 7 April 2020) to retrieve the data that is needed. We run the WRF model for the specific cases we study for situations when AROME data is not available. TAPM (Hurley, 2008; Hurley et al., 2005) is a prognostic meteorological and air pollution model that can be used to create meteorological input for EPISODE; please consult Part Two of this paper for more details on TAPM and an example of its application (Karl et al., 2019).

The MCWIND utility produces a diagnostic wind field and other meteorological fields for the defined model grid, by first constructing an initial first-guess wind field based on the measurements of the horizontal wind and vertical temperature differential at two or more meteorological stations. Then the horizontal 2-D fields are interpolated to the 3-D grid of the model domain by applying Monin-Obukhov similarity theory. Finally, the first-guess 3-D wind field is adjusted to the given topography by requiring the resulting wind field in each model layer to be non-divergent and mass-consistent.

The meteorological inputs have to be provided on the 3D spatial gridding used by the EPISODE model, which is defined in the EPISODE input runfile. Thus, in the case of the AROME, WRF, TAPM, and MCWIND, these external models and utilities have to be run at the same spatial resolution as the planned EPISODE simulations. In most applications EPISODE is run at 1 × 1 km horizontal resolution but has been run at 200 m × 200 m resolution. The typical vertical resolution used is such that the layer adjacent to the surface is 24 m thick, there are 20 layers within the first km, 8 layers between 1 and 2 km in altitude, and a further 7 beyond that up to 3.5 km. The meteorological inputs are typically provided at hourly intervals and have been done

so for all current and recent applications. However, the interval can be set to different times depending on the limitations of the input meteorological data.

2.4 Pre-Processing Utilities

Several pre-processing utilities are used in conjunction with the EPISODE model. These utilities are used for preparing
5   meteorological inputs, emissions files, and boundary condition files used in the running of an EPISODE simulation. The pre-processing utilities are:

1. CAMSBC (collection of routines to convert CAMS regional production to EPISODE background input). The CAMS regional data can be used as background pollutant concentrations and can downloaded directly from the CAMS online data portal (CAMS online data portal: https://atmosphere.copernicus.eu/data, last access: 7 April 2020).

10   2. UECT (interface for line source, point source, and area source emissions allows use of EPISODE independent of AirQUIS).

3. TAPM4CC (interface to convert TAPM meteorology output when TAPM is used as a source of meteorological input);

4. Utilities to generate auxiliary input.

Table 3 gives an overview of the purpose of the pre-processing utilities as well as outlining the input and output formats and
15   descriptions.

3 Case Study Description and Model Setup

As a demonstration and validation of EPISODE's capabilities we carry out the simulations of NO_2 concentration levels over six Norwegian cities. The chosen urban areas are Oslo, Trondheim, Stavanger, Drammen, Grenland (including the city of Skien), and Nedre Glomma (encompassing both Fredrikstad and Sarpsborg on the Glomma river). The model domains for
20   these urban areas are shown in Figure 3. The EPISODE model is run for the entire year of 2015 using meteorological input from the AROME model, which was run operationally over the six city domains by the Norwegian Meteorological Institute (Denby and Süld, 2015). The AROME model simulations are carried out at 1×1 km horizontal spatial resolution on the exact same gridding and domain as the EPISODE model simulations for each city. The AROME meteorological outputs are provided every hour and are read into EPISODE at the same frequency. Further details of the meteorological fields used in EPISODE
25   are documented in S7 of the supplement. AROME provides NetCDF files for input, and the surface roughness and topography used in AROME were extracted from these files.

The NO_x emissions used for the simulations for each of the six city domains were developed as part of the NBV project (Tarrasón et al., 2017). The methodologies for the creation of the emission datasets are described in (Lopez-Aparicio & Vo, 2015). The data sources, methodology, and emission reference years are summarized in Table 4 for sector.
30   Different approaches were used to compile the emission datasets depending on the data availability for the specific emission sector. On-road traffic emissions are estimated based on a bottom-up traffic emission model. The traffic emission model

16

produces emissions for each road link. It takes into account traffic volume (i.e., average daily traffic, ADT) and heavy duty fraction of the traffic on specific road types (e.g., highway, city street, etc.). In addition, the emission model considers the road slope. This information is obtained from the Norwegian Road Administration. The ADT is combined with temporal profiles of daily traffic to obtain hourly ADT at the road level. The vehicle fleet composition is defined as a fraction of each vehicle

5   technology class (EURO standard) and fuel type, which combined with the HBEFA emission factors and the hourly fraction of ADT, results in emissions on each road segment. The information regarding the vehicle technology class is obtained from regional statistics (Opplysningsrådet for Veitrafikken, 2013).

Emissions from non-road mobile machinery in construction, industry and agriculture were originally produced by Statistics Norway, spatially distributed at the district level and thereafter gridded at 1×1 km resolution. The previous data stems from

10   different years in each model domain: Drammen from 2012; Oslo from 1995; in Stavanger from 1998; and Trondheim from 2005. Non-road mobile machinery is not available in Grenland and Nedre Glomma.

For all cities except Oslo, emissions from shipping are obtained from the Norwegian Coastal Administration based upon the automatic identification system (AIS) following the methodology of (Winther et al., 2014). In the case of Oslo, emissions were estimated following a bottom-up approach based on the port activity registering system (López-Aparicio et al., 2017). This

15   includes detailed information on arrivals, departures and operating times for individual vessels. Industrial emissions were originally provided by Statistics Norway. Industrial emissions are usually linked to the geographical position of large point sources. In the case of Grenland and Nedre Glomma sufficient information (i.e., emission rate, location, stack height and diameter, flue gas speed, and plume temperature) on industrial point sources existed to be able to represent these pollution sources as point sources and to calculate their buoyancy driven plume rise. However, when achieving this level of detail this

20   was not possible for industrial sources, as in the case for Oslo, Stavanger, Trondheim, and Drammen, they were distributed spatially based on surrogate data, as e.g. employment figures in the industrial sector. Finally, for some locations (e.g., Grenland; Table 4), the original dataset of industrial emissions was outdated. In this case, emissions were evaluated and updated based on information from the Norwegian Pollutant Release and Transfer Register.

25

Table 5 describes how each sector is represented by the different possible emission types, e.g., line or area sources and presents the ratios between NO and NO_2 for the NO_x emissions. The fraction of NO_2 in emitted NO_x (as NO_2 mass equivalent) varies between 4.5% and 45.9% depending on the source.

30   The initial and background hourly concentrations used in the simulations are obtained from the CAMS regional air quality forecast production system (Marécal et al. 2015). The NetCDF files containing NO, NO_2, and ozone for a domain covering all of Norway and all vertical levels (0 m, 50 m, 250 m, 500 m, 1000 m, 2000 m, 3000 m, and 5000 m) came from the CAMS online data portal: https://atmosphere.copernicus.eu/data (last access: 7 April 2020). The CAMS regional forecast data is

selected for each city domain, and then interpolated horizontally and vertically to the gridding used in EPISODE. In this case study, we used the 34 vertical levels shown in Table 6. Table 6 also gives information on the size of each model domain, and the number of receptor points used.

4 Results and Evaluation of Model Performance

5 ## 4.1 Mapping and Evaluation of Annual and Seasonal Model Results

4.1.1 Annual Mean Concentration Mapping

Annual mean NO_2 concentrations are relevant for air quality mapping since the 2008/50/EC directive (AQD) defines an annual mean NO_2 concentration limit value of 40 µg/m^3. We therefore present annual mean NO_2 concentration maps for four out of the six model domains as demonstration of EPISODE's application: Oslo (Figure 4), Drammen (Figure 5), Nedre Glomma

10 (Figure 6), and Grenland (Figure 7). The four selected cities represent the general features that we see in each domain, cover all of the types of simulated spatial variability, and, therefore, provide a representative sample of the whole.

A primary aim behind the development of EPISODE was to create a model capable of mapping air pollution at high spatial resolution at scales relevant for human exposure within urban areas. We apply a post-processing methodology (outlined in Appendix B, the Pollution Mapping Post-Processing Methodology) to the irregularly spaced receptor points in order to create

15 the pollution maps for each city on a regular 100 m grid. Note that this post-processing method is only applied for visualisation purposes and that for model evaluation (see Sect. 4.1.2) and exposure assessment purposes, the receptor point concentrations (C_{rec}) are used directly.

The most notable features of the spatial patterns present in all of the maps are the elevated concentrations along the principal segments of the road network and main intersections. For example, the motorway E18 is visible in the Oslo domain (Figure 4)

20 running in the east-west direction along the Oslo fjord, in the Drammen domain (Figure 5) running in the north-south direction on the right-side of the map and in the Grenland domain (Figure 7) in the southeast corner of the domain. In addition, the E6, another motorway, is visible in Oslo running north-south to the east of the fjord and in Nedre Glomma (Figure 6) running north-south on the east side of the map. Also visible are district roads like the ones to the east of Oslo (RV 4, RV163 and RV 159) and the road N234 along the north of Drammensfjorden. This reflects the main source for NO_X emissions in Norwegian

25 cities: traffic. Oslo has the largest population and largest number of commuters, and this is reflected in the largest hotspot area of concentrations ≥40 µg/m^3 of the four presented maps.

Another notable feature of elevated NO_2 pollution on the maps are what appear to be point source emissions: in Oslo in the southernmost region of the domain along the E6 (59.74° N,10.82° E) (Figure 5) and in Drammen at 59.738° N, 10.16° E and 59.73° N, 10.22° E (Figure 6). These elevated levels are due to emissions from tunnel mouths. In the Oslo this is the north/south

30 entrances of the Nøstvet Tunnel on the E6, and in Drammen the east/west entrances of the Strømså Tunnel. The tunnel mouth emissions are prescribed by creating road segments at either end with elevated traffic levels.

Oslo and Drammen are characterized by annual mean sub-urban NO_2 concentrations of 10-20 µg m^{-3}. Oslo with higher emissions shows higher background concentrations with a smoother gradient from the city centre to the forested areas with concentrations in the range 0-5 µg m^{-3}. Despite Drammen having similar levels of population to the cities in Nedre Glomma and Grenland, it still shows some relatively high NO_2 concentrations compared to these two domains. This is because Drammen sits on the primary commuting route between Oslo and cities to the west, and thus has significant commuting traffic.

Both the Nedre Glomma and the Grenland model domains have populations divided in two main agglomerations: Sarpsborg and Fredrikstad and Porsgrunn and Skien, respectively. This leads to NO_2 annual mean concentrations in the city centres and suburban areas lower than either Oslo or Drammen. In Nedre Glomma (Figure 6) the annual average NO_2 concentrations of the background outside of the urban areas and away from the main roads. The background mean NO_2 concentration in this area does not fall below 5 µg m^{-3} because the rural areas in this domain are actually mostly farmland with many off-road service roads that support farmland. This means there is much greater off-road activity and off-road emission sources in this area compared to the other domains.

One aspect of the Grenland domain is the prevalence of industrial pollution sources. Industry is concentrated on the Herøya peninsula at the mouth of the Posrgrunnselva river (in the centre of the domain), and on the western side of the fjord in the southern half of the domain. Mean annual NO_2 concentrations are somewhat elevated in these areas with values ~25 µg m^{-3}. The industrial emissions are treated as stack emissions injected into model layers tens of meters above the surface due to their plume buoyancy and the stack height. This explains why their impact is seen as a more diffuse zone of pollution around the industrial areas.

4.1.2 Full-Year and Seasonal Model Evaluation

We evaluate the year-long NO_2 simulations for 2015 for all six domains (Oslo, Drammen, Grenland, Nedre Glomma, Stavanger and Trondheim) using in-situ air quality observations of NO_2. Both the model and observation data will be evaluated in hourly format and unless otherwise stated. Due to its size and population Oslo has an increased regulatory requirement to monitor its pollution and it is therefore the most well sampled city with a total of eight in-situ measurement sites compared to only two at most in the other domains. A receptor point is placed at the coordinate and height of each in-situ station shown in Table 7. The simulated concentrations at these receptor points are then used in the evaluation.

We present Taylor diagrams to evaluate the model results compared to the in-situ observations. Taylor diagrams visually represent the results of three statistical tests (Pearson correlation coefficient, the root-mean-square error, and the ratio of the model standard deviation compared to the observed standard deviation) in a simultaneous fashion. The Taylor diagrams provide a good overall indication of the model performance purely from a statistical standpoint.

Figure 8 shows the results of the statistical tests for the year-long simulation during 2015. Looking at the σM/σO ratios, we see in general, that the model captures the amplitude of NO_2 concentration variability reasonably well across all but one of the stations (Våland) with a range in σM/σO from 0.62 to 1.40. There is neither a tendency of the model to either over or underestimate σ with almost an equal number of stations above and below 1.0. Only Våland (Stavanger) shows a high spread

in modelled NO_2 concentrations compared to the observations with a σM/σO ratio of 1.67. We can rule out the effect of a persistent bias at Våland since the model shows only a small positive bias (+ 1.64 µg m^{-3}) with respect to these observations. Instead, this overestimate in the dynamic range appears to be linked to an overestimation in the NO_2 diurnal variability during summer. It is possible this is due to an error in the emission magnitude and variability local to Våland during summer time.

5   The comparison with the Kannik station, also in Stavanger, supports this notion since it shows a value of σM/σO much closer to 1.0 than for Våland. All but one of the sixteen in-situ stations score values of R between 0.5 and 0.67 with only Kannik scoring lower than 0.5 at 0.49. The RMSE ranges between 0.77 µg m^{-3} and 1.18 µg m^{-3} for fifteen out of the sixteen stations. Only Våland has a much higher RMSE at 1.45 µg m^{-3}, which is linked to its high σM/σO ratio. The results of each statistical test for each station are shown in the Taylor diagrams (Figure 8, Figure 9, and Figure 10) and are summarised in

10

15

Table 8. The mean values of R, RMSE, and σM/σO for all sixteen stations are 0.6, 0.96 µg m^{-3}, and 1.06, respectively. This characterises the general model performance.

    We next evaluate the EPISODE model simulations using only data from the wintertime (January, February, and December

20   combined). We carry out this specific evaluation in order to test the EPISODE model under conditions where the PSS approximation is likely fulfilled. The PSS is expected to be a reasonable approximation for conditions lacking local photochemical ozone production such as during winter in Nordic environments. Figure 9 shows the results of this evaluation in a Taylor diagram. Evaluating the model solely during winter conditions leads to a substantial improvement in model performance scores. Now fourteen out of sixteen in-situ stations score with R values above 0.6 peaking up to 0.69. Only the

25   stations Elgeseter (Trondheim) and Øyekast (Grenland) score below 0.6 both with values of 0.58. Excluding Våland (Stavanger), which has a σM/σO ratio of 1.42, the σM/σO ratios range between 0.54 to 1.23 for the remaining stations. Please refer to the earlier discussion of Figure 8 regarding the high modelled NO_2 concentration variability at Våland. Compared to the evaluation of the annual results, the winter-time results show lower values of σM/σO and a tendency of the model to underestimate the standard deviation of the NO_2 concentrations. The temporal variability (not shown) indicates that the stations

30   with the lowest σM/σO, i.e., Manglerud, Kirkeveien, Bygdøy Alle, Hjortnes and Alnabru in Oslo, and Elgeseter in Trondheim, all tend to underestimate peak daytime NO_2 concentrations. The RMSE is reduced overall for the sixteen stations: the RMSE

20

ranges between 0.74 μg m^{-3} and 1.00 μg m^{-3} with only Våland showing and an RMSE of 1.09 μg m^{-3} for similar reasons as explained earlier. The mean winter-time statistics are shown in

5

10 Table 8, which demonstrate a notable improvement in performance compared to the annual statistics. We also checked the statistics during the autumn (no figures shown) and see an improved performance during the period September 1st to November 30th (see

15

20 Table 8) relative to the rest of the year and the summer.

The expectation is that the PSS should provide a reasonable approximation of NO$_2$ photochemistry during the winter months. This seems to be supported here by the improved statistics that we see during wintertime compared to the entire year. Furthermore, experiments in part two (Karl et al., 2019) comparing the PSS to the more comprehensive EmChem09 chemical mechanism (70 compounds, 67 thermal reactions and 25 photolysis reactions) show that it performs adequately within the 25 vicinity of NO$_x$ sources. However, despite these encouraging results, the PSS does not include N$_2$O$_5$ formation and subsequent hydrolysis to form HNO$_3$. These reaction pathways are an important sink for NO$_x$ during the night (Dentener and Crutzen, 1993), and this is therefore an important limitation of the PSS.

We present evaluation results only for the summertime in the Taylor diagram shown in Figure 10. We see a notable degradation in model performance in terms of R and RMSE for all stations. In addition, half of the model stations show anomalously high 30 σM/σO ratio with values of 1.3 or above. We attribute this poorer model performance to the lack of photochemical production of NO$_2$ and ozone represented in the PSS chemistry scheme, without this process we should expect a different diurnal variability in NO$_2$ concentrations from that observed. Even in Oslo, we expect ozone production during the summer months.

5

10   Table 8 shows the mean statistics for the thirteen stations shown in Figure 10, and the R and RMSE statistics show an overall degraded performance relative to the annual and winter-time evaluations.

We next evaluate the model performance using the DELTA tool target plots (Monteiro et al., 2018; Thunis and Cuvelier, 2018; Thunis et al., 2012). These plots offer a means of evaluating different aspects of model performance directly on the axes of the plots, i.e., normalised bias and the centred root mean square error (CRMSE), on the x and y-axes, respectively. The DELTA

15   Tool plots also offer a means to evaluate the model within the context of the EC Directive while also considering the observation uncertainty. Thus, this type of evaluation offers a different perspective from the statistical measures in the Taylor diagram evaluations. Further details of the DELTA Tool method consult Appendix C and the references above. The position of a particular model-observation pair (individual points show the results for single stations) in each quadrant tells about which type of error dominates over the other. Specifically, correlation error expressed as R dominates over standard deviation error

20   in the left quadrants, and vice-versa in the right quadrants. Meanwhile, points in the upper quadrants indicate positive model bias and the contrary in the lower quadrants. Additionally, the tool uses the CRMSE and normalised bias to calculate a target value, which is also visualised on the target plot as the distance from the origin. The objective is to have points with a target value of 1 or less and thus lie within the green area of the plots.

Separately, the DELTA tool calculates the model quality indicator (MQI) (see Appendix C and enclosed references for further

25   details), which determines whether the model-observation bias is less than the observation uncertainty. Furthermore, Monteiro et al. (2018) and Thunis and Cuvelier (2018) define the model quality objective (MQO) as to whether the 90th percentile of MQI for all stations is less than 1. If this criterion is satisfied the model quality objective is satisfied.

Figure 11, Figure 12, and Figure 13 show the target plots for the year-round evaluation, the winter-time only evaluation, and the summer-time only evaluation, respectively. The target plots highlight an important and consistent feature of the model

30   performance throughout the year, which is that all of the model-observation evaluation pairs lie in the upper and lower left-hand quadrants. This indicates the correlation error, expressed as R, dominates the contribution to the CRMSE error term.

We first discuss the annual evaluation shown in Figure 11. The MQO is satisfied for the annual evaluation with the 90th percentile of the MQI calculated at 0.971. Only one station, Bygdøy Alle, has a large enough negative bias to have a specific

MQI value above 1. Overall, an equal number of stations have a positive and negative normalised bias. However, there is an apparent signal in the Oslo results for a negative bias in this evaluation, and the magnitude of the negative biases is slightly larger than the positive biases.

EPISODE achieves the MQO during winter with the 90th percentile of MQI being calculated at 0.995. This is despite two
5 stations in Oslo, Åkebergveien and Bygdøy Alle, showing larger than acceptable low biases during the winter-time period. Both stations are visible in the lower left quadrant outside of the green target zone. Given the reasonable correlations at both stations, we can perhaps infer that a persistent model or emission process is the cause of this effect. Further study will be required to determine in detail the cause of this, but one possibility is the current lack of a specific consideration of cold engine starts that have a tendency to increase NO_x emissions from vehicle sources during wintertime. Such an explanation would be
10 consistent with the overall bias evaluation in the target plot where we see that there are more stations with a negative bias than a positive bias. Similarly as in Figure 11, the magnitude of the negative bias is larger than the magnitude of the positive bias, and, similarly, it is the Oslo stations that have a greater tendency to show a negative bias. We note that the MQO is also satisfied during the autumn (figure not shown) with the 90th percentile of the MQI being calculated at 0.996.

Despite the degraded performance shown in the Taylor diagram for the summer in Figure 10, the MQO is satisfied for the
15 summer time analysis with the 90th percentile MQI being calculated at 0.933. Please note the exclusion of the Kannik and Våland stations due to lack of data. Following guidelines from the EC air quality Directive, neither had sufficient observations during the summer to be able to perform the DELTA tool target plot analysis. Despite this limitation, we can show that the MQO is satisfied across the thirteen remaining stations indicating that the model bias is consistently low enough at these locations on an hour by hour basis. The overall bias statistics show no strong prevalence for a negative or positive bias, but, as
20 before, the magnitude of the negative bias slightly larger and we see a negative bias affecting the Oslo stations in preference to the other cities.

4.2 The Model's Capability of Capturing Pollution Episodes

We now present examples of EPISODE mapping NO_2 during pollution events. We select two periods of interest for Oslo and Drammen where NO_2 concentrations became elevated over a few days. The first is an event that took place in Oslo between
25 December 9th and 13th, and the second took place in Drammen between January 4th and 7th. We analyse each event using daily mean maps from the worst day of the pollution event, time series for selected stations, and statistical scores for the available stations.

4.2.1 Oslo Pollution Episode 10th-13th December 2015

Figure 14 is a plot of the time series for the observed and modelled NO_2 concentrations at two measuring sites in Oslo
30 (Åkebergveien and Manglerud) throughout the duration of the event. These two stations are selected because they exhibit different characteristics of the pollution episode with different timings for the onset, and the model exhibits different performance statistics for each station (see Table 9). The pollution event began on 10th December with a period of relatively

mild temperatures and moderate south westerly winds; at this point a peak in NO_2 (> 60 µg m^{-3}) is only visible at Manglerud (and other stations in the west of Oslo). On the 11th there was a transition into colder conditions with very light southerly winds that coincided with a worsening of the pollution episode as seen in Figure 14 at Åkebergveien. The model captures this difference at both stations. Further, the model captures the shorter duration of the peak in NO_2 concentrations at Manglerud on December 10th compared to the other days. The cold and light wind conditions persisted for the remainder of the pollution event. For further details on the meteorological conditions for the period 9th to 13th December and for a comparison between the meteorological input to EPISODE and observations, please consult the supplement S8.

Figure 15 shows a map of the daily mean NO_2 concentrations over the Oslo domain for December 11th. The map shows significant elevated NO_2 concentrations over large areas of the domain. Average levels of 40 µg m^{-3} and higher were present over most of the urban areas in and around the city with levels of 60 µg m^{-3} and higher present in the central and eastern areas of Oslo and along major roads outside the city. On December 11th effect of the southerly winds are clearly visible in the form of plumes to the north of roads running east-west to the east of Oslo.

In Table 9 we can see that the σM/σO ratio is lower than 1.0 for all comparisons against in-situ stations. Looking at Figure 14 we can see that the model captures the night-time minima reasonably well, but underestimates peak NO_2 concentrations. This underestimate of the peak is either due to uncertainties in boundary layer meteorology, the emissions magnitude, or time variability of the emissions. Further study will be required to determine the exact cause. Overall, these scores demonstrate acceptable model performance during this pollution episode. This highlights that EPISODE can capture individual pollution events when coupled with meteorological forcing and background pollutant concentrations of sufficient quality.

4.2.2 Drammen Pollution Episode 4th-7th January 2015

We display the time series of the observed and modelled receptor point NO_2 concentrations for Bangeløkka in Figure 16. Details on the meteorological situation are presented in the supplement S8. The onset of the event (> 60 µg m^{-3}) started on the afternoon of 4th January during a period of light westerly winds with temperatures close to zero degrees Celsius. The pollution worsened (> 100 µg m^{-3}) on 5th January during a colder period with very low wind speeds. From January 6th onwards there was no clear wind direction but with more moderate wind speeds. Notably, on 6th January the input meteorology overestimates the wind speed, which leads to an underestimate in the peak NO_2 concentration that day. Further details on the meteorological situation are presented in the supplement S8.

Figure 17 shows a map of the mean NO_2 concentrations over Drammen for January 5th when the worst pollution occurred. EPISODE simulates concentrations of 30 µg m^{-3} and higher over much of the populated areas in and around Drammen along the Drammenselva river and to the North and South of the fjord along the E18 highway. Only the settlement of Konnerud (in the south-central area of the domain) avoided levels over 30 µg m^{-3}.

Evaluating the model performance against the Bangeløkka in-situ station in Drammen we find that the ratio of the modelled and observed standard deviation, σM/σO, was 0.82, indicating lower than observed model variability. The Pearson correlation, R, was 0.8, the RMSE was equal to 0.59 µg m^{-3}, and the mean bias was +4.3 µg m^{-3}. The model captures the extent of the

nighttime minimum in NO_2 concentrations (0/24h to 6h) on two out of four occasions, but does not capture the full extent of the maximum on three out of four days (this is linked to an overestimate of the wind speed on 6th January). Unfortunately, we only have one in-situ station available to evaluate the model in the Drammen domain for this pollution episode, which prevents a wider evaluation. Within this limitation, the statistics show acceptable model performance at one of the most polluted sites in Drammen. This again highlights that when coupled with meteorological forcing of acceptable quality and background concentrations of pollutants, EPISODE can capture individual pollution events sufficiently well.

5 Summary

The EPISODE urban dispersion model was presented, which serves as the base model for the EPISODE-CityChem extension described in Part 2 of this paper (Karl et al., 2019). EPISODE combines a 1×1 km 3D Eulerian grid with sub-grid scale dispersion from point and line sources to receptor points. This allows EPISODE to provide a finer scale and higher resolution representation of pollution in urban environments than regional chemistry transport models. It thus addresses one of the main weaknesses of regional air quality models, i.e., the recurring problem of representing a diverse range of urban environments (from street-side to urban background) all within a 10+ km scale grid. We presented here the simulation of NO_2 pollution at high resolution using a PSS chemistry scheme consisting of NO_2, NO, and O_3. This scheme was designed to simulate NO_2 pollution in Nordic low-sunlight environments where its usage was considered appropriate. The EPISODE-CityChem extension in Part 2 includes a more comprehensive chemistry scheme suitable for a wider range of environments. We demonstrate the application of EPISODE in six case studies in Norwegian cities for the entire year of 2015. We evaluated the model against in-situ observations of NO_2 concentrations in all six cities, and present more traditional statistical metrics including RMSE, R, and σM/σO (the ratio of simulated and observed standard deviations), and dedicated metrics for evaluating air quality models, e.g., target plot analysis and a model quality objective (Monteiro et al. 2018; Thunis and Cuvelier 2018; Thunis et al., 2012). The model satisfies the model quality objective for every time period it was evaluated for (annual, winter, autumn, and summer), and only two stations out of sixteen failed the target plot analysis. The statistics over the whole year demonstrate an overall reasonable performance throughout the year. However, more in-depth analysis of the model performance during the different seasons demonstrates significantly improved performance, both in terms of correlation and RMSE, during autumn and winter compared to summer. The degraded performance of the model during summer is a strong indication of the limitations of the PSS during such conditions. This is consistent with the expectation that the PSS chemistry should perform well during the darker months of the year in polluted environments. The findings in part two of this paper series (Karl et al., 2019) comparing the PSS and EmChem09 chemical mechanisms also support this. Together, these findings demonstrate the suitability of EPISODE for studying the NO_2 pollution problem within urban environments in Norway since the most elevated NO_2 pollution levels occur during autumn and winter. For this application, we conclude that EPISODE is suitable both for scientific study of NO_2 air pollution and also to support policy applications, e.g., NO_2 pollution episode analysis, seasonal statistics, policy and planning support, and air quality management.

6 Future Work

We outline several developments that are planned in the near future aimed at improving the representation of NO_2 in EPISODE simulations. The first is to simulate the entrainment of ozone within NO_x-rich plumes from traffic emissions. Currently, the PSS is solved at each receptor point using the NO and NO_2 transported from the pollution sources and the grid ozone. We propose replacing the current treatment of ozone and include a simulation of ozone mixing into the NO_x-rich plumes linked to the stability conditions.

Another weakness of the PSS is that it solves the chemistry to equilibrium instantaneously regardless of the distance of a receptor point from a pollution source. When in reality, the equilibrium between NO_2, NO, and ozone may take minutes to achieve. On the short transport timescales of only tens of meters from a pollution source, this may be problematic and a treatment of the chemistry accounting for the time to reach equilibrium and the transport distance may be more appropriate. We plan to modify the PSS calculations to account for this type of situation.

Lastly, we plan to introduce another modification to the photostationary steady state that will simulate the formation of N_2O_5, which is an important winter-time sink for NO_x (Dentener and Crutzen, 1993). This will require the introduction of the chemical species NO_3 and N_2O_5 itself into the photostationary steady state scheme. N_2O_5 loss onto aerosols will be considered via an uptake coefficient onto a dynamically calculated particulate matter surface area derived from the simulation of particulate matter concentrations.

We are planning to carry out a comprehensive and focused evaluation of the new urban Kz method described in Sect. 2.2.1 in a dedicated separate study in the near future. This is dependent on obtaining suitable observations, which we plan on gathering at the earliest opportunity.

It is already possible to simulate particulate matter concentrations for $PM_{2.5}$ and PM_{10} with the EPISODE model (in separate simulations from the NO_2 runs), but we chose not to present case studies for these pollutants in this paper. Compared to NO_2, the current model uncertainties for simulating $PM_{2.5}$ and PM_{10} are linked much more to emission processes, i.e., wood burning and road dust resuspension, respectively. Both emission processes require dedicated models external to EPISODE to estimate realistic emissions, which are beyond the scope of this paper. Running without the inclusion of these emission processes results in significantly degraded model performance compared to the NO_2 simulations. The standalone emission models are the MEDVED model for wood burning emissions (Grythe et al., 2019), and the NORTRIP model for road dust resuspension (Denby et al. 2013). The offline coupling of both emission models into EPISODE for PM simulations is planned and will greatly enhance the model's capability for simulating particulate matter pollution. In addition to this, a standalone traffic exhaust emission model is being developed that will replace many of the functionalities of the AirQUIS system.

To further enhance the simulation of PM within the model, we plan to soon implement PM removal processes, i.e., below cloud wet scavenging and sedimentation. We will also implement size bins for PM, which will improve the representation of PM removal processes that are affected by particle size, e.g., impaction, diffusion, and interception.

To further benchmark the EPISODE model, it would be interesting to perform an intercomparison with other urban scale air quality models using identical inputs for a particular case study. The evaluation could then be made using a standardised and accepted evaluation method, e.g., DELTA tool (Monteiro et al., 2018).

5 *Code and data availability:* The source code for the EPISODE model version 10 is available under the RPL 1.5 license at https://doi.org/10.5281/zenodo.3244056. The model compilation requires installation of the gcc/gfortran fortran90 compiler (version 4.4. or later) and the netCDF library (version 3.6.0 or later).

Model input datasets are available from the NILU ftp server upon request. These datasets include: meteorological, emission, and ancillary input files for the entire year 2015; output model data for all of the 2015 simulations; and data in the format for
10 the DELTA Tool analysis package.

Appendix A: Emission Input Method

Area Gridded Emissions

The units of the emissions are in g s^{-1}, and in the case of NO and NO$_X$ this is in terms of the mass of NO$_2$ equivalent. The input
15 format for the area source emissions is ASCII.

Line Source Emissions

The line source emissions are described in two ASCII input files. The first file describes the road links giving the UTM coordinates of the road link beginning and end points, the width, the height at the beginning and end points, and the area of influence, R$_{inf}$, around a road link. The second contains the hourly total emission intensity along each road link, E$_R$, in terms
20 of gs^{-1}.m for each time step of the simulation. Road link emissions are assumed to be evenly distributed along a single road link.

Point Source Emissions

The point source emission files are in ASCII format and contain the following information for each stack: their hourly emission rates in gs^{-1}, the geographical location of the stack in UTM coordinates, the building width and height, the stack height and
25 diameter, the temperature of the plume gas, and the speed at which the plume is expelled from the chimney.

Appendix B: Pollution Mapping Post-Processing Methodology

The visualisation in the maps is created by first subtracting from each receptor point concentration, C$_{rec}$, the Eulerian grid concentration, C$_m$, for the corresponding grid square in which the receptor point resides following,

$$C_{local} = C_{rec} - C_m \quad (A1)$$

30 which leaves the local concentration residual, C$_{local}$. Next, the Eulerian grid concentration field at 1 km resolution, Cm, is interpolated to the coordinates, $(x^r, y^r, 1)$, of each receptor point using a spline method to give, C$_{m,rec}$, following

$$Cm,rec = F_{int}(Cm, [x^r, y^r]) \quad (A2)$$

Then both the residual from Eq. (A1) and $C_{m,rec}$ are added together to determine the receptor point concentration, C_{rec*}, which now contains both the receptor point and the interpolated Eulerian grid components. Finally, the modified concentrations for all of the irregularly spaced receptor points, C_{rec*}, are then re-gridded onto a 100 x 100 m grid covering the entire domain using tri-linear interpolation.

5   In practice, there are many areas within the urban centre with receptor point sampling at higher spatial resolutions than 100 m. Thus, 100 m represents a conservative choice for the effective mapping resolution in these important areas. This post-processing step also serves to remove the visual imprint of the 1 x 1 km Eulerian grid (remember that receptor point concentrations are a sum of the Eulerian grid and local contribution following Eq. (7) from the gridded receptor point concentrations.

10   **Appendix C: Statistical indicators and model performance indicators**

The model is evaluated with the following statistical metrics: the ratio of the modelled and observed standard deviation ($\sigma M/\sigma O$), root mean squared error (RMSE), centred root mean square error (CRMSE), Pearson's correlation coefficient (R), normalised mean bias (NMB), and index of agreement (IOA).

The respective standard deviations of the model and observations are calculated via

15   $$\sigma M = \sqrt{\frac{1}{N} \sum_{i=1}^{N}(M_i - \bar{M})^2} \qquad \text{(B1)}$$

$$\sigma O = \sqrt{\frac{1}{N-1} \sum_{i=1}^{N}(O_i - \bar{O})^2} \qquad \text{(B2)}$$

The RMSE provides a representation of the magnitude of the error for each hourly model-observation pair and is defined as (RMSE shares the units of the variables being evaluated, i.e., in this case µg m^{-3}):

$$RMSE = \sqrt{\frac{1}{N} \sum_{i=1}^{N}(M_i - O_i)^2} \qquad \text{(B3)}$$

20   $$R = \frac{\frac{1}{N}\sum_{i=1}^{N}(M_i - \bar{M})(O_i - \bar{O})}{\sigma M \, \sigma O} \qquad \text{(B4)}$$

The IOA is defined as

$$IOA = 1 - \frac{\sum_{i=1}^{N}(M_i - O_i)^2}{\sum_{i=1}^{N}(|M_i - \bar{M}| + |O_i - \bar{O}|)^2} \qquad \text{(B5)}$$

When the IOA is equal to 1 it indicates perfect agreement between the model and observations and a value of zero indicates no agreement at all.

25   The CRMSE and normalised mean bias are used in the axes of the DELTA Tool target plots and are calculated as follows:

$$CRMSE = \sqrt{\frac{1}{N}\sum_{i=1}^{N}((O_i - \bar{O}) - (M_i - \bar{M}))^2} \qquad \text{(B6)}$$

$$NMB = \frac{\bar{M} - \bar{O}}{\bar{O}} \qquad \text{(B7)}$$

In addition to these metrics, we also evaluate the model according to the DELTA Tool model quality indicator (MQI) and the related model quality objective (MQO) (Monteiro et al., 2018; Thunis and Cuvelier, 2018). The MQI calculation provides an advanced evaluation of model performance by considering the observation uncertainty on each individual measurement, $U_{95}(O_i)$, which is defined as:

$$U_{95}(O_i) = k\, u_r^{RV} \sqrt{(1 - \alpha^2)O_i^2 + \alpha^2 (RV)^2} \qquad \text{(B8)}$$

Where u_r^{RV} is the relative measurement uncertainty estimated around a reference value, RV, for a given time averaging, e.g., hourly or daily limit values of the air quality directive. α^2 is the fraction of the uncertainty around RV, which is non-proportional to the concentration level, and k is the coverage factor that scales the error in order to achieve a specific confidence interval. k is most typically set to 2 in order to achieve a 95% confidence interval.

The root mean square of the observation error is calculated via:

$$RMS_U = \sqrt{\frac{1}{N}\sum_{i=1}^{N}(U_{95}(O_i))^2} \qquad \text{(B9)}$$

The MQI is then define as the ratio between the absolute model-observation bias and a quantity proportional to the observation uncertainty via:

$$MQI = \frac{|O_i - M_i|}{\beta\, RMS_U} \qquad \text{(B10)}$$

Where β is a scaling set to 2 in the DELTA Tool. In the DELTA Tool target plots, MQI is the distance between the origin and a point on the plot for a given station. The MQO is considered fulfilled when MQI ≤ 1. Following the Air Quality Directive requirements, the DELTA Tool sets a criteria whereby the MQO is defined as being satisfied when the MQI is fulfilled for at least 90% of the stations. In other words, ranking the station MQIs in ascending order, the inferred 90th percentile must be 1 or lower.

Author contributions.

PDH: wrote the main text of the paper; developed a technical description of the model based on an in-depth evaluation of the code; developed the scientific questions; ran the model case studies for the six Norwegian cities; analysed and evaluated the EPISODE model results presented in this work.

SEW: implemented the HIGHWAY-2 line source dispersion model and the two point source dispersion models in EPISODE.

GSS: Supported scientific design of the six city case studies and made significant developments to EPISODE code, e.g., development of coupling with AROME meteorological data.

PS: post-processed the EPISODE model results and visualized the results as the maps.

MV: post-processed the EPISODE model results and visualized the results as the maps.

DVT: prepared the emissions used in the EPISODE model runs.

SAL: provided the technical and scientific guidance for the preparation of the emissions used in the EPISODE model runs.

References

10   Baldasano, J., Pay, M., Jorba, O., Gassó, S. and Jimenez-Guerrero, P.: An annual assessment of air quality with the CALIOPE modeling system over Spain, Sci. Total Environ., 409, 2163–2178, 2011.

Benavides, J., Snyder, M., Guevara, M., Soret, A., Pérez Garc\'\ia-Pando, C., Amato, F., Querol, X. and Jorba, O.: CALIOPE-Urban v1.0: Coupling R-LINE with a mesoscale air quality modelling system for urban air quality forecasts over Barcelona city (Spain), Geosci. Model Dev. Discuss., 2019, 1–35, doi:10.5194/gmd-2019-48, 2019.

15   Bengtsson, L., Andrae, U., Aspelien, T., Batrak, Y., Calvo, J., de Rooy, W., Gleeson, E., Hansen-Sass, B., Homleid, M., Hortal, M., Ivarsson, K.-I., Lenderink, G., Niemelä, S., Nielsen, K. P., Onvlee, J., Rontu, L., Samuelsson, P., Muñoz, D. S., Subias, A., Tijm, S., Toll, V., Yang, X. and Køltzow, M. Ø.: The HARMONIE–AROME Model Configuration in the ALADIN–HIRLAM NWP System, Mon. Weather Rev., 145(5), 1919–1935, doi:10.1175/MWR-D-16-0417.1, 2017.

Bott, A.: A Positive Definite Advection Scheme Obtained by Nonlinear Renormalization of the Advective Fluxes, Mon.
20   Weather Rev., 117(5), 1006–1016, doi:10.1175/1520-0493(1989)117<1006:APDASO>2.0.CO;2, 1989.

Bott, A.: Monotone Flux Limitation in the Area-preserving Flux-form Advection Algorithm, Mon. Weather Rev., 120(11), 2592–2602, doi:10.1175/1520-0493(1992)120<2592:MFLITA>2.0.CO;2, 1992.

Bott, A.: The monotone area-preserving flux-form advection algorithm: reducing the time-splitting error in two-dimentional flow fields, Mon. Weather Rev., 121(9), 2637–2641, doi:10.1175/1520-0493(1993)121<2637:TMAPFF>2.0.CO;2, 1993.

25   Briggs, G. A.: Plume rise, U.S. Atomic Energy Commission, Oak Ridge Tennessee., 1969.

Briggs, G. A.: Some recent analyses of plume rise observation, in Proceedings of the Second International Clean Air Congress, edited by H. M. E. and W. T. Berry, pp. 1029–1032, Academic Press, New York., 1971.

Briggs, G. A.: Diffusion estimation for small emissions, Atmos. Turbul. Diffus. Lab., 83, 1974.

Briggs, G. A.: Plume rise predictions, lectures on air pollution and environment impact analysis, Am. Meteorol. Soc., Boston,
30   USA, 10, 1975.

Byun, D. and Schere, K. L.: Review of the governing equations, computational algorithms, and other components of the Models-3 Community Multiscale Air Quality (CMAQ) modeling system, Appl. Mech. Rev., 59(2), 51–77, 2006.

Denby, B. R. and Süld, J. K.: METreport NBV report on meteorological data for 2015 METreport, , (January 2010), 2015.

Denby, B. R., Sundvor, I., Johansson, C., Pirjola, L., Ketzel, M., Norman, M., Kupiainen, K., Gustafsson, M., Blomqvist, G. and Omstedt, G.: A coupled road dust and surface moisture model to predict non-exhaust road traffic induced particle emissions (NORTRIP). Part 1: Road dust loading and suspension modelling, Atmos. Environ., 77, 283–300, 2013.

5   Denby, B. R., Sundvor, I., Høiskar, B. A. K. and Kristensen, A.: Bedre byluft 2016 - Forskningsresultater og utvikling av prognoser for meteorologi og luftkvalitet i norske byer 2016, Oslo., 2017.

Dentener, F. J. and Crutzen, P. J.: Reaction of N2O5 on tropospheric aerosols: Impact on the global distributions of NO x, O3, and OH, J. Geophys. Res. Atmos., 98(D4), 7149–7163, 1993.

Endregard, G.: AirQUIS: A modern air quality management tool, Nor. Inst. air Res., 2002.

10   EU: Directive 2008/50/EC of the European Parliament and of the Council of 21 May 2008 on ambient air quality and cleaner air for Europe, Off. J. Eur. Communities, 152, 1–43, doi:http://eur-lex.europa.eu/LexUriServ/LexUriServ.do?uri=OJ:L:2008:152:0001:0044:EN:PDF, 2008.

Fagerli, H., Tsyro, S., Denby, B. R., Gauss, M., Simpson, D., Wind, P., Benedictow, A., Jonson, J. E., Klein, H., Schulz, M., Griesfeller, J., Aas, W., Hjellbrekke, A., Solberg, S., Platt, S. M., Fiebig, M., Yttri, K. E., Rud, R. O., Mareckova, K., Pinterits,

15   M., Tista, M., Ullrich, B., Posch, M., Imhof, H., Putaud, J., Cavalli, F., Poulain, L., Schlag, P., Heikkinen, L. M., Swietlicki, E., Martinsson, J., Vana, M., Smejkalova, A. H., Kouvarakis, G. and Mihalopoulos, N.: No Title, n.d.

Fedra, K. and Haurie, A.: A decision support system for air quality management combining GIS and optimisation techniques, Int. J. Environ. Pollut., 12(2–3), 125–146, 1999.

Foley, K. M., Roselle, S. J., Appel, K. W., Bhave, P. V., Pleim, J. E., Otte, T. L., Mathur, R., Sarwar, G., Young, J. O., Gilliam,

20   R. C., Nolte, C. G., Kelly, J. T., Gilliland, A. B. and Bash, J. O.: Incremental testing of the Community Multiscale Air Quality (CMAQ) modeling system version 4.7, Geosci. Model Dev., 3(1), 205–226, doi:10.5194/gmd-3-205-2010, 2010.

Franke, J., Hellsten, A., Schlunzen, K. H. and Carissimo, B.: The COST 732 Best Practice Guideline for CFD simulation of flows in the urban environment: a summary, Int. J. Environ. Pollut., 44(1–4), 419–427, 2011.

Grythe, H., Lopez-Aparicio, S., Vogt, M., Vo Thanh, D., Hak, C., Halse, A. K., Hamer, P. and Sousa Santos, G.: The MetVed

25   model: Development and evaluation of emissions from residential wood combustion at high spatio-temporal resolution in Norway, Atmos. Chem. Phys. Discuss., 2019, 1–33, doi:10.5194/acp-2019-95, 2019.

Irwin, J. S.: Estimating Plume Dispersion-A Comparison of Several Sigma Schemes, J. Clim. Appl. Meteorol., 22(1), 92–114, doi:10.1175/1520-0450(1983)022<0092:EPDACO>2.0.CO;2, 1983.

Jensen, S. S., Berkowicz, R., Sten Hansen, H. and Hertel, O.: A Danish decision-support GIS tool for management of urban

30   air quality and human exposures, Transp. Res. Part D Transp. Environ., 6(4), 229–241, doi:10.1016/S1361-9209(00)00026-2, 2001.

Karl, M., Walker, S.-E., Solberg, S. and Ramacher, M. O. P.: The Eulerian urban dispersion model EPISODE. Part II: Extensions to the source dispersion and photochemistry for EPISODE-CityChem v1.2 and its application to the city of Hamburg, Geosci. Model Dev. Discuss., 2019, 1–62, doi:10.5194/gmd-2018-325, 2019.

Lateb, M., Meroney, R. N., Yataghene, M., Fellouah, H., Saleh, F. and Boufadel, M. C.: On the use of numerical modelling for near-field pollutant dispersion in urban environments - A review, Environ. Pollut., 208, 271–283, doi:10.1016/j.envpol.2015.07.039, 2016.

Lopez-Aparicio, S. and Vo, D. T.: Emission estimates for Norwegian cities. NBV_Emission Database v.0. Norsk institutt for luftforskning (NILU), Kjeller. [online] Available from: https://www.nilu.no/DesktopModules/NiluWeb.UserControls/Resources/File.ashx?filename=35-2015-NBV_DeliverableAP2_D3_accepted-rnh.pdf&filetype=file, 2015.

López-Aparicio, S., Tønnesen, D., Thanh, T. N. and Neilson, H.: Shipping emissions in a Nordic port: Assessment of mitigation strategies, Transp. Res. Part D Transp. Environ., 53, 205–216, 2017.

Mar??cal, V., Peuch, V. H., Andersson, C., Andersson, S., Arteta, J., Beekmann, M., Benedictow, A., Bergstr??m, R., Bessagnet, B., Cansado, A., Ch??roux, F., Colette, A., Coman, A., Curier, R. L., Van Der Gon, H. A. C. D., Drouin, A., Elbern, H., Emili, E., Engelen, R. J., Eskes, H. J., Foret, G., Friese, E., Gauss, M., Giannaros, C., Guth, J., Joly, M., Jaumouill??, E., Josse, B., Kadygrov, N., Kaiser, J. W., Krajsek, K., Kuenen, J., Kumar, U., Liora, N., Lopez, E., Malherbe, L., Martinez, I., Melas, D., Meleux, F., Menut, L., Moinat, P., Morales, T., Parmentier, J., Piacentini, A., Plu, M., Poupkou, A., Queguiner, S., Robertson, L., Rou??l, L., Schaap, M., Segers, A., Sofiev, M., Tarasson, L., Thomas, M., Timmermans, R., Valdebenito, Van Velthoven, P., Van Versendaal, R., Vira, J. and Ung, A.: A regional air quality forecasting system over Europe: The MACC-II daily ensemble production, Geosci. Model Dev., 8(9), 2777–2813, doi:10.5194/gmd-8-2777-2015, 2015.

McRae, G. J., Goodin, W. R. and Seinfeld, J. H.: Development of a second-generation mathematical model for urban air pollution—I. Model formulation, Atmos. Environ., 16(4), 679–696, 1982.

Monteiro, A., Durka, P., Flandorfer, C., Georgieva, E., Guerreiro, C., Kushta, J., Malherbe, L., Maiheu, B., Miranda, A. I., Santos, G. and others: Strengths and weaknesses of the FAIRMODE benchmarking methodology for the evaluation of air quality models, Air Qual. Atmos. Heal., 11(4), 373–383, 2018.

Opplysningsrådet for veitrafikken: Kjøretøystatistikk 2013, Oslo., 2013.

Pay, M. T., Piot, M., Jorba, O., Gass??, S., Gon??alves, M., Basart, S., Dabdub, D., Jim??nez-Guerrero, P. and Baldasano, J. M.: A full year evaluation of the CALIOPE-EU air quality modeling system over Europe for 2004, Atmos. Environ., 44(27), 3322–3342, doi:10.1016/j.atmosenv.2010.05.040, 2010.

Pergaud, J., Masson, V., Malardel, S. and Couvreux, F.: A parameterization of dry thermals and shallow cumuli for mesoscale numerical weather prediction, Boundary-layer Meteorol., 132(1), 83, 2009.

Petersen, W. B.: User's guide for HIWAY-2. A highway air pollution model., 1980.

Petersen, W. B. and Lavdas, L. G.: INPUFF 2. 0-a multiple-source Gaussian puff dispersion algorithm. User's guide. Final report., 1986.

Seity, Y., Brousseau, P., Malardel, S., Hello, G., Bénard, P., Bouttier, F., Lac, C. and Masson, V.: The AROME-France convective-scale operational model, Mon. Weather Rev., 139(3), 976–991, 2011.

Simpson, D., Andersson-Skøld, Y. and Jenkin, M. E.: Updating the chemical scheme for the EMEP MSC-W oxidant

model:current status, Oslo. [online] Available from: https://emep.int/publ/reports/1993/EMEP_1993_N2.pdf, 1993.

Simpson, D., Benedictow, A., Berge, H., Bergstr??m, R., Emberson, L. D., Fagerli, H., Flechard, C. R., Hayman, G. D., Gauss, M., Jonson, J. E., Jenkin, M. E., Ny??ri, A., Richter, C., Semeena, V. S., Tsyro, S., Tuovinen, J. P., Valdebenito, A. and Wind, P.: The EMEP MSC-W chemical transport model – Technical description, Atmos. Chem. Phys., 12(16), 7825–7865, doi:10.5194/acp-12-7825-2012, 2012.

Sivertsen, B. and Bøhler, T.: On-line Air Quality Management System for Urban Areas in Norway, air our cities--it's everybody's business". Paris, 16–18, 2000.

Skamarock, W. C., Klemp, J. B., Dudhia, J., Gill, D. O., Liu, Z., Berner, J., Wang, W., Powers, J. G., Duda, M. G., Barker, D. M. and Huang, X.-Y.: A Description of the Advanced Research WRF Version 4, NCAR Tech. Note NCAR/TN-556+STR, 145, doi:doi:10.5065/1dfh-6p97, 2019.

Slørdal, L. H., Solberg, S. and Walker, S.-E.: The Urban Air Dispersion Model EPISODE applied in AirQUIS2003, Technical description, Kjeller, Norway., 2003.

Slørdal, L. H., McInnes, H. and Krognes, T.: The Air Quality Information System AirQUIS, Info. Techn, Environ. Eng, 1, 21–33, 2008a.

Slørdal, L. H., McInnes, H. and Krognes, T.: The air quality information system AirQUIS, Environ. Sci. Eng, 1, 40–47, 2008b.

Smith, G. D.: Numerical solution of partial differential equations: finite difference methods, Clarendon Press, Oxford, UK., 1985.

Tarodo, J.: Continuous emission monitoring, Tarodo, J, 34, 67–72, 2003.

Tarrasón, L., Santos, G. S., Thanh, D. V., López-aparicio, S., Denby, B. and Tønnesen, D.: Air quality in Norwegian cities in 2015., 2017.

Thunis, P.; Cuvelier, C.: DELTA Version 5.6 Concepts / User's Guide / Diagrams, Ispra., 2018.

Thunis, P., Pederzoli, A. and Pernigotti, D.: Performance criteria to evaluate air quality modeling applications, Atmos. Environ., 59, 476–482, 2012.

Walker, S.E. and Grønskei, K. .: Spredningsberegninger for on-line overvåking i Grenland. Programbeskrivelse og brukerveiledning, Lillestrøm., 1992.

World Health Organization: Ambient Air Pollution: A global assessment of exposure and burden of disease, World Heal. Organ., 1–131, doi:9789241511353, 2016.
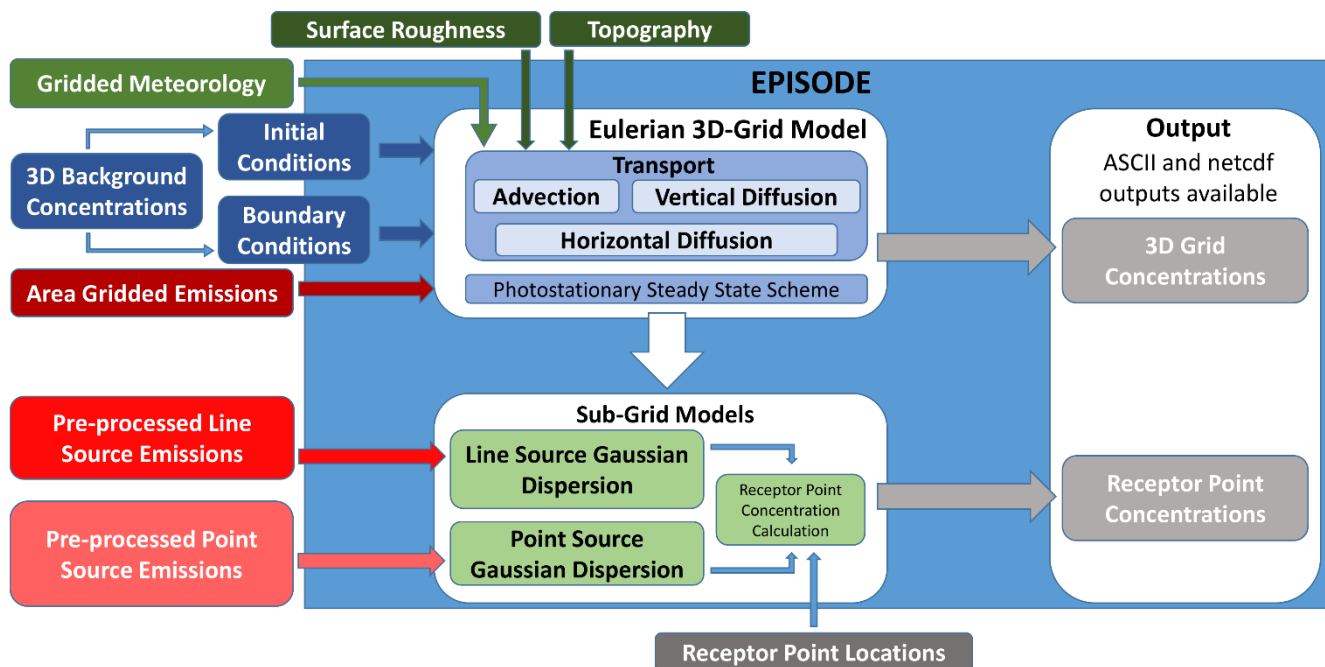
Figure 1. Schematic diagram of the EPISODE model. The large blue box represents operations carried out during the execution of the EPISODE model. The components of the EPISODE model are the Eulerian grid model and the sub-grid models. The inputs for EPISODE are specified on the periphery.
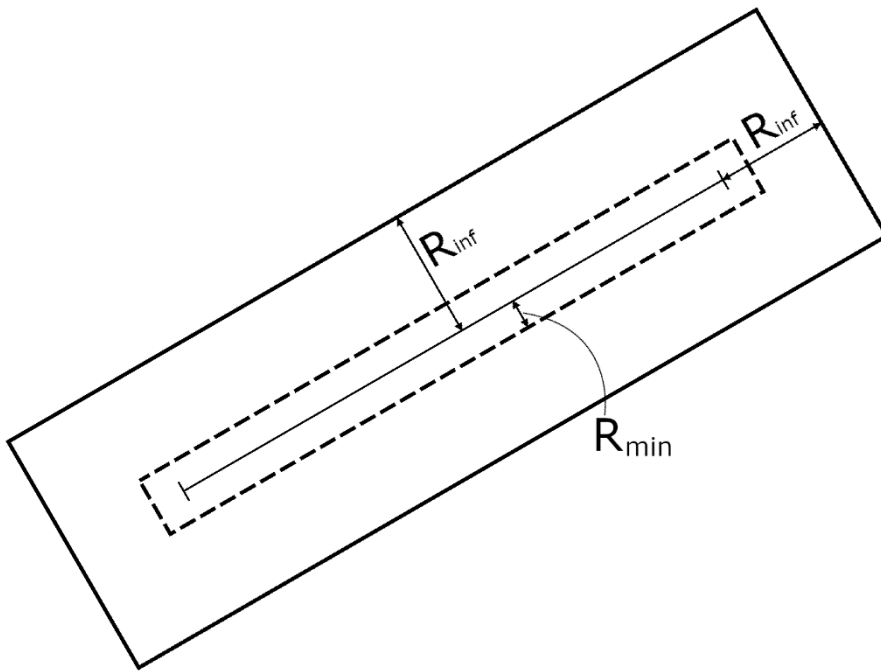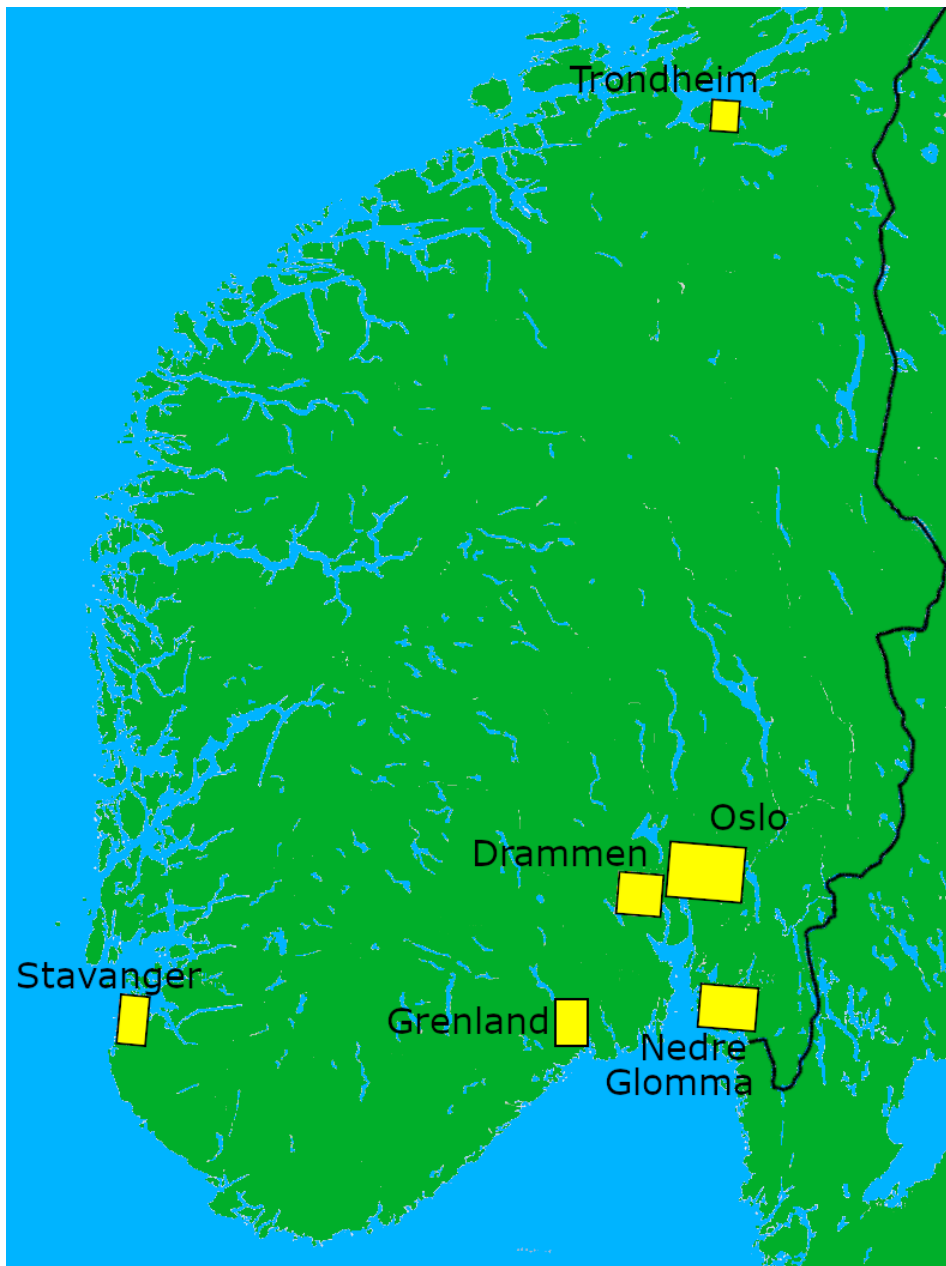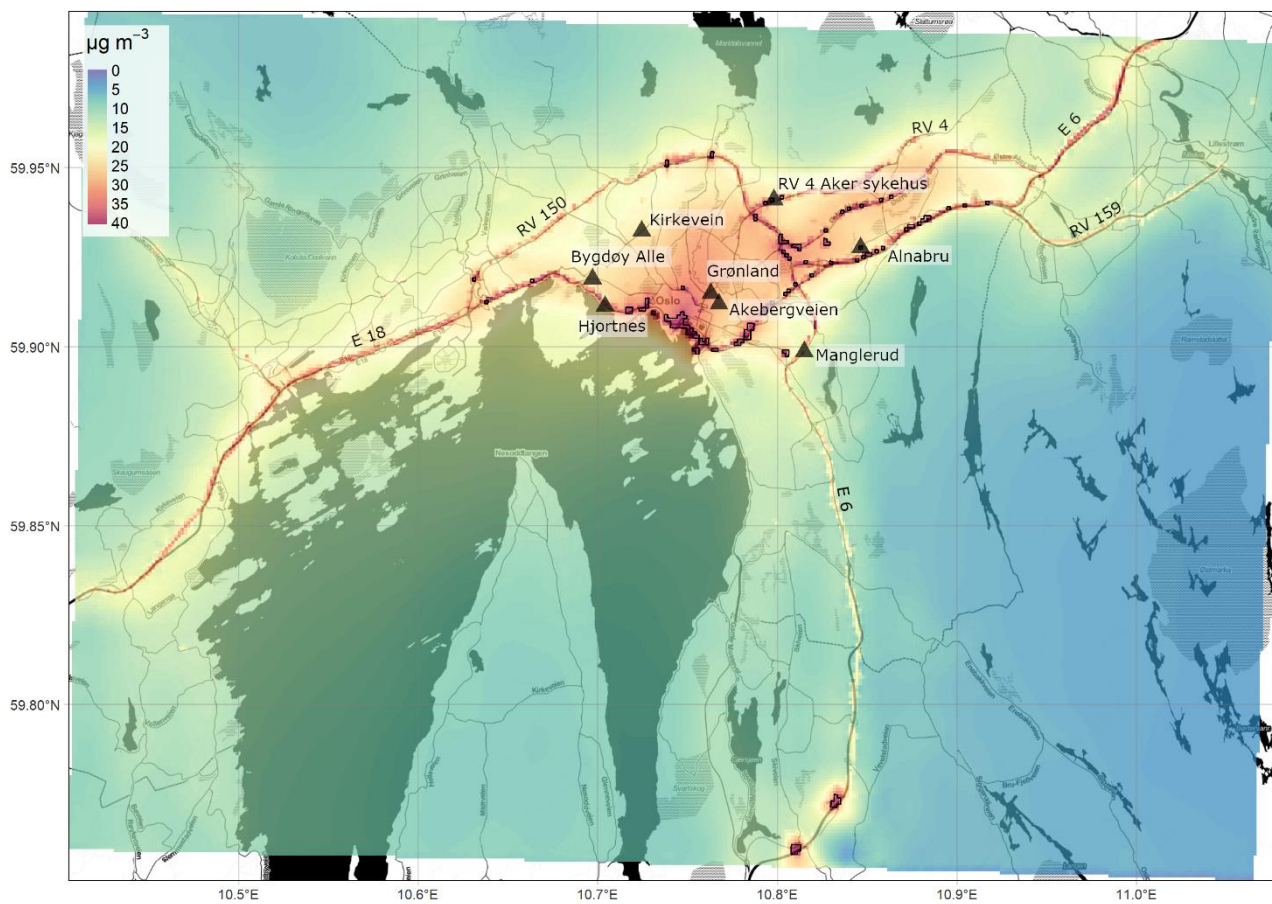
5

Figure 2. An illustration of the rectangular area of influence around an example road link showing the minimum (R_{min}) and maximum (R_{inf}) distances influenced by a line source.

Figure 3. A Map of the southern part of Norway showing the location and extent of the six modelling domains Stavanger, Trondheim, Grenland, Drammen, Oslo, and Nedre Glomma.

5

Figure 4. Annually averaged NO$_2$ concentrations (µg/m^3) from the EPISODE model over the Oslo domain at 100 m x 100 m horizontal resolution. The concentrations are derived from the receptor point concentrations and then re-gridded onto a 100 m grid. The colour scale shows the range in annual mean NO$_2$ concentrations between 0 and 40 µg m^{-3}. The black triangles indicate the locations of the air quality observation stations (Table 7). The dark shaded areas represent the sea, lakes and rivers. The black lines are roads. © OpenStreetMap contributors 2019. Distributed under a Creative Commons BY-SA License.
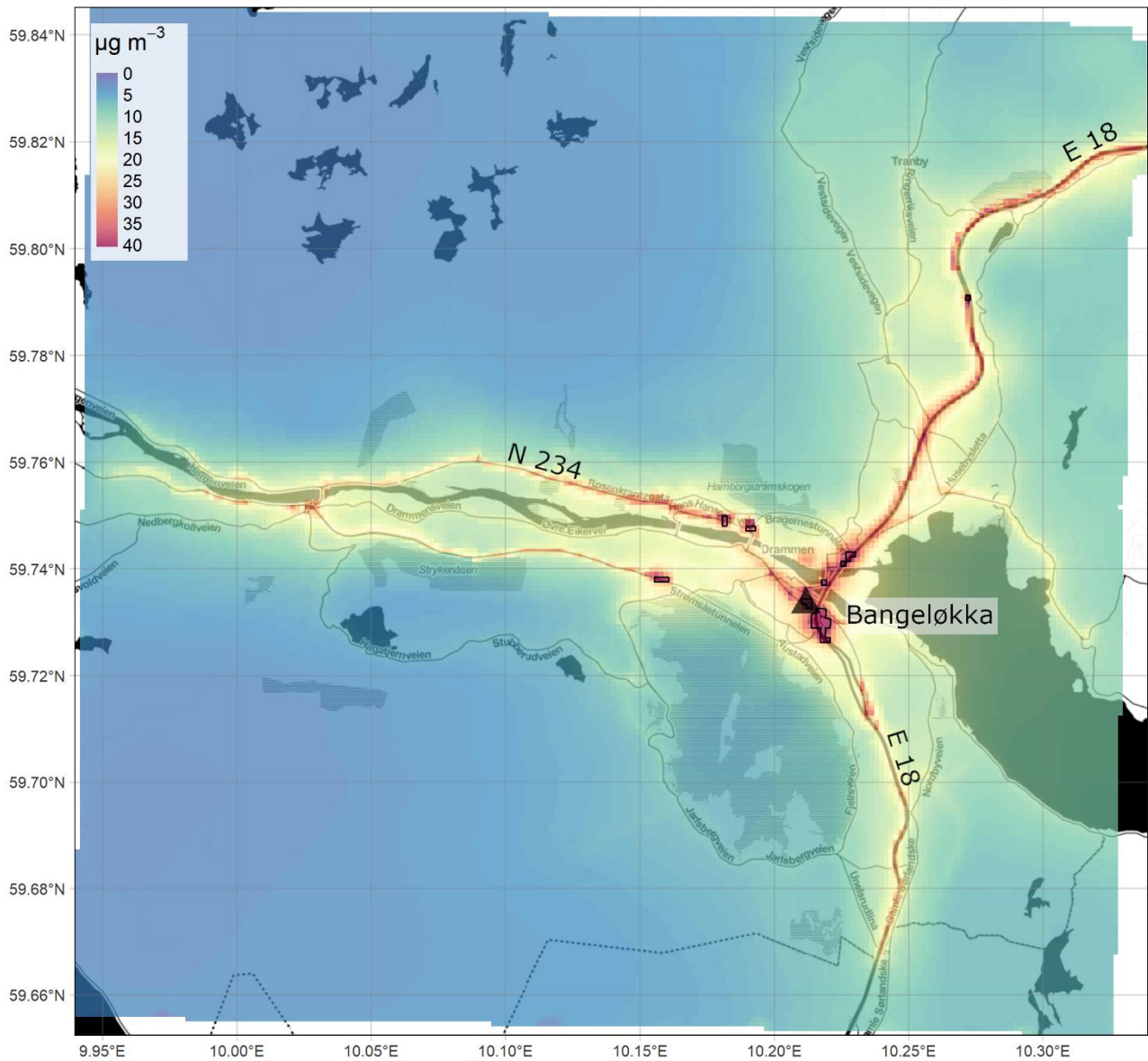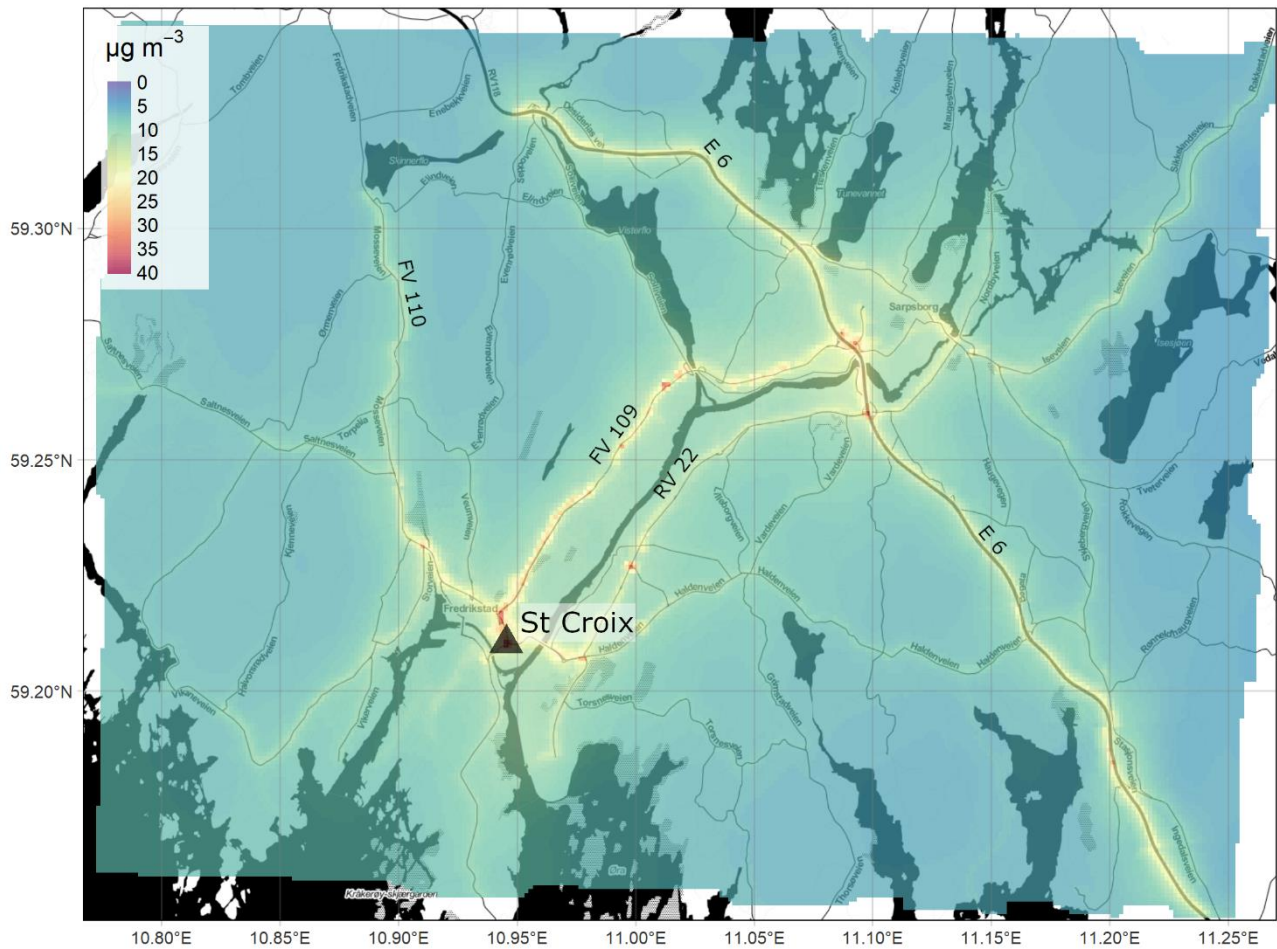
Figure 5. **Annually averaged NO₂ concentrations (μg/m³) from the EPISODE model over the Drammen domain at 100 m x 100 m horizontal resolution. The concentrations are derived from the receptor point concentrations and then re-gridded onto a 100 m grid. The colour scale shows the range in annual mean NO₂ concentrations between 0 and 40 μg m⁻³. The black triangles indicate the locations of the air quality observation stations (Table 7). The dark shaded areas represent the sea, lakes and rivers. The black lines are roads. © OpenStreetMap contributors 2019. Distributed under a Creative Commons BY-SA License.**
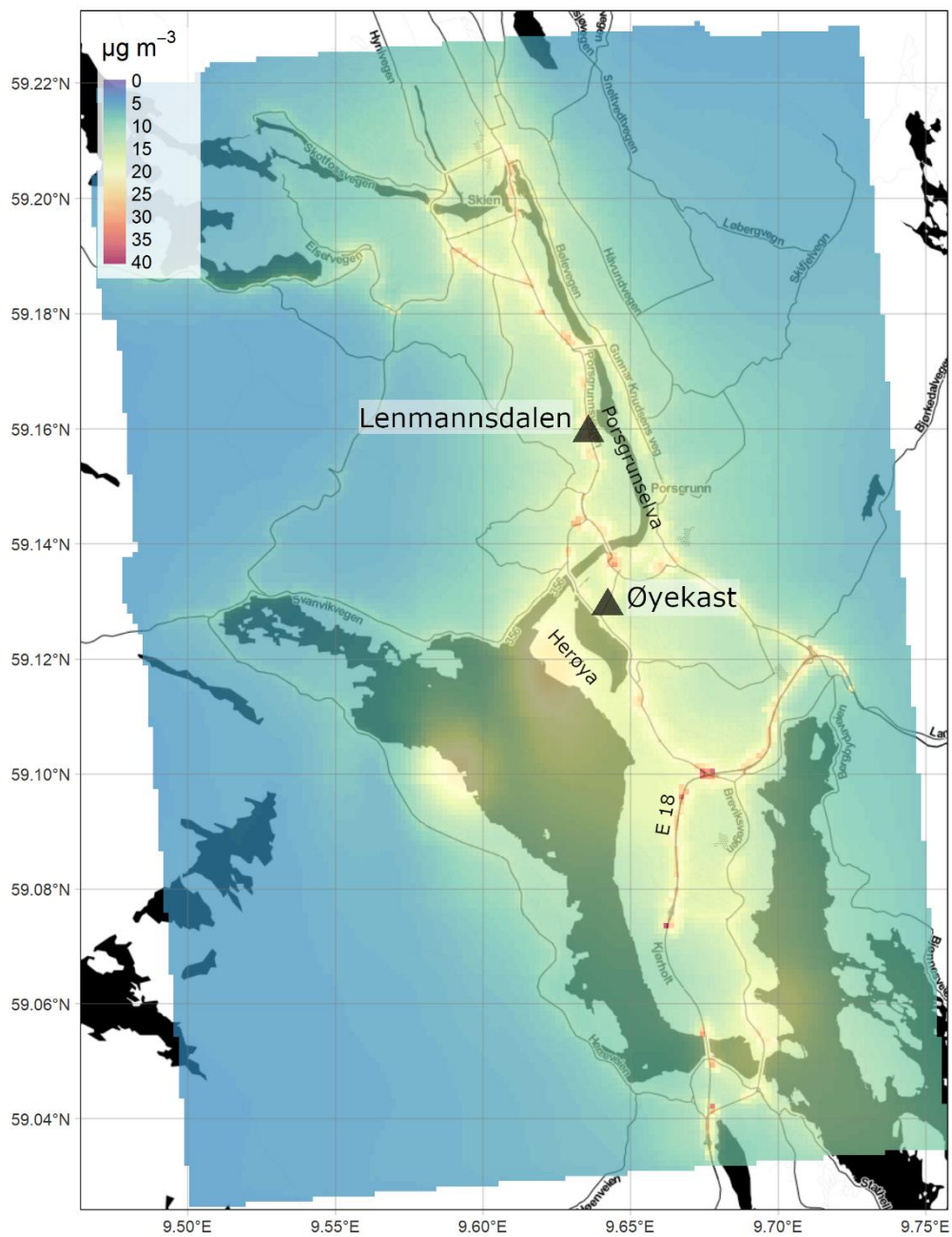
Figure 6. Annually averaged NO₂ concentrations (μg/m³) from the EPISODE model over the Nedre Glomma domain at 100 m x 100 m horizontal resolution. The concentrations are derived from the receptor point concentrations and then re-gridded onto a 100 m grid. The colour scale shows the range in annual mean NO₂ concentrations between 0 and 40 μg m⁻³. The black triangles indicate the locations of the air quality observation stations (Table 7). The dark shaded areas represent the sea, lakes and rivers. The black lines are roads. © OpenStreetMap contributors 2019. Distributed under a Creative Commons BY-SA License.
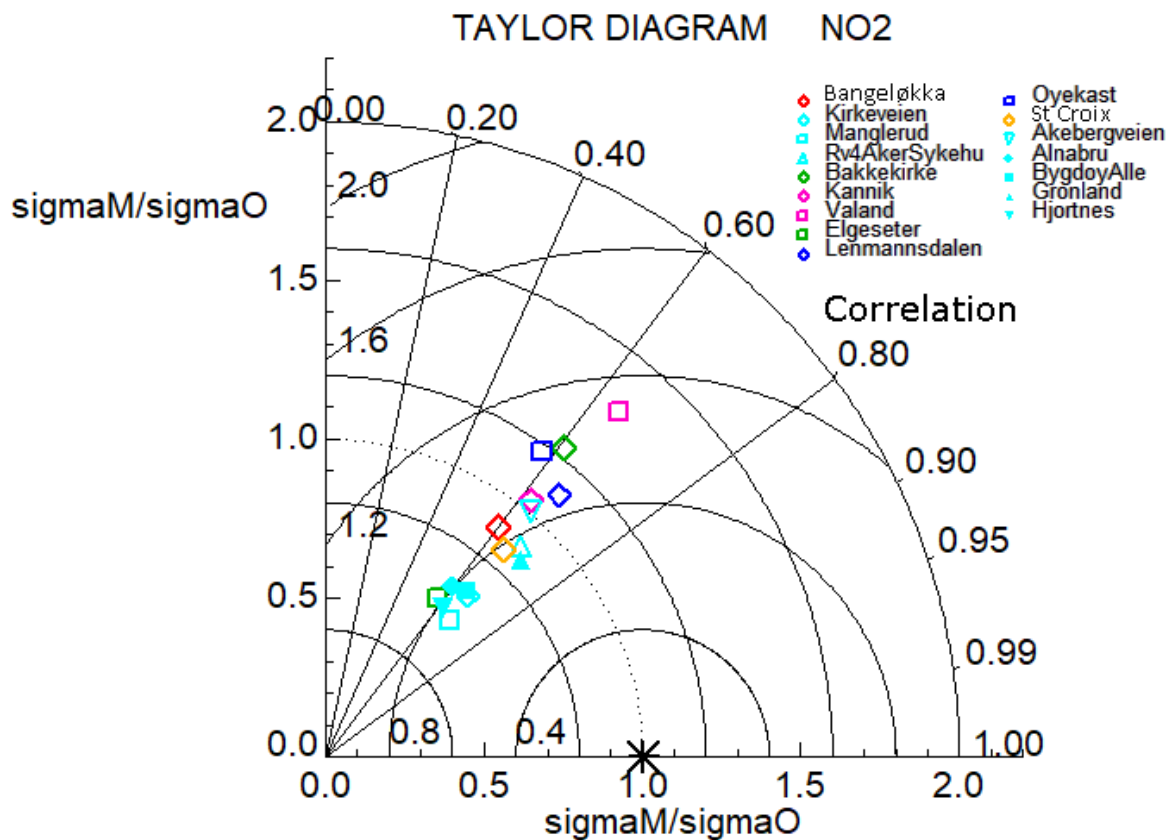
Figure 7. Annually averaged NO₂ concentrations (μg/m³) from the EPISODE model over the Grenland domain at 100 m x 100 m horizontal resolution. The concentrations are derived from the receptor point concentrations and then re-gridded onto a 100 m grid. The colour scale shows the range in annual mean NO₂ concentrations between 0 and 40 μg m⁻³. The black triangles indicate the locations of the air quality observation stations (Table 7). The dark shaded areas represent the sea, lakes and rivers. The black lines are roads. © OpenStreetMap contributors 2019. Distributed under a Creative Commons BY-SA License.
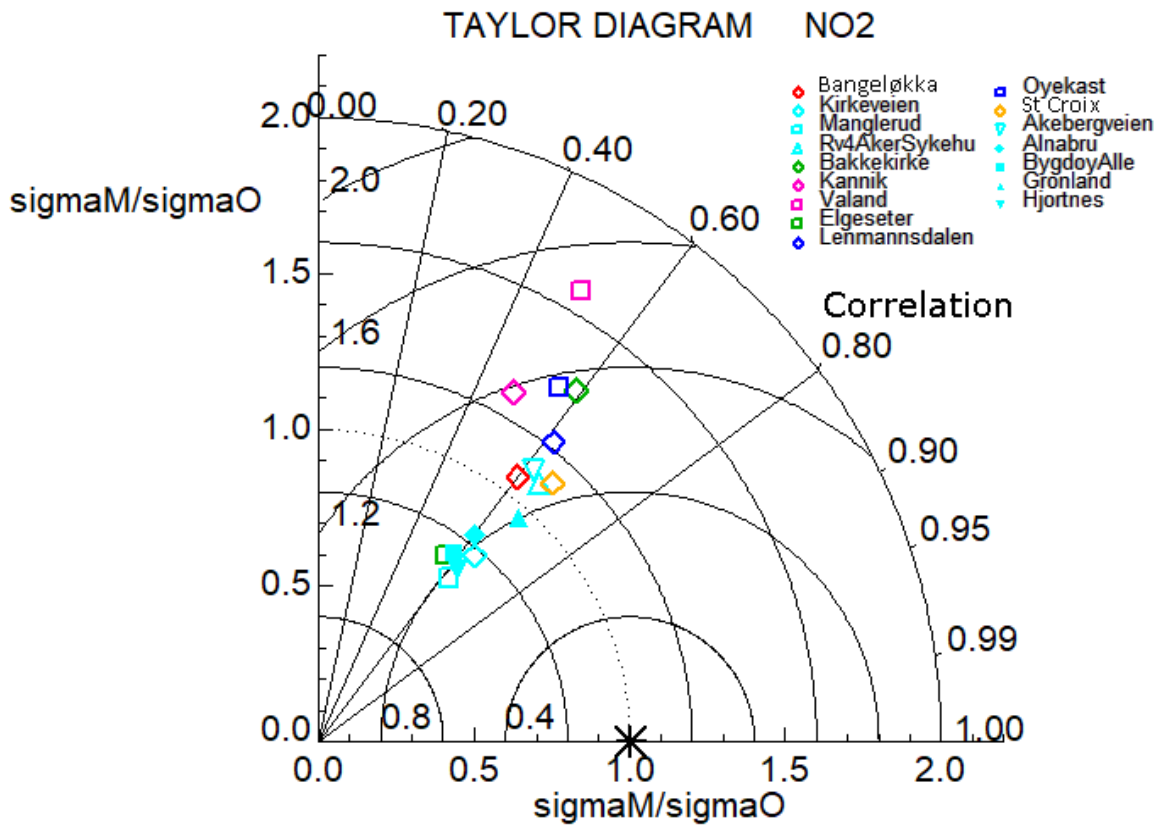
Figure 8. A Taylor diagram calculated using the annual hourly time series of NO_2 concentrations for all sixteen in-situ stations used for the model evaluation across all six domains. The symbols are colour coded according to each model domain where Drammen is red, Oslo is cyan, Trondheim is green, Stavanger is pink, Grenland is dark blue, and Nedre Glomma is orange. The x and y-axis both represent the ratio of the model standard deviation to the observed standard deviation in NO_2 concentrations for a particular station, such that points can be plotted on concentric circles centred on the x/y origin. The correlation is plotted according to the azimuthal angle from the origin represented as a series of straight lines emanating from the x/y origin. Lastly, the RMSE (units µg m⁻³) is also represented for each station according to their linear distance from 1.0 on the x-axis.

Figure 9. A Taylor diagram calculated using the winter only (January, February, and December) hourly time series of NO₂ concentrations for all sixteen in-situ stations used for the model evaluation across all six domains. The symbols are colour coded according to each model domain where Drammen is red, Oslo is cyan, Trondheim is green, Stavanger is pink, Grenland is dark blue, and Nedre Glomma is orange. The x and y-axis both represent the ratio of the model standard deviation to the observed standard deviation in NO₂ concentrations for a particular station, such that points can be plotted on concentric circles centred on the x/y origin. The correlation is plotted according to the azimuthal angle from the origin represented as a series of straight lines emanating from the x/y origin. Lastly, the RMSE (units μg m⁻³) is also represented for each station according to their linear distance from 1.0 on the x-axis.
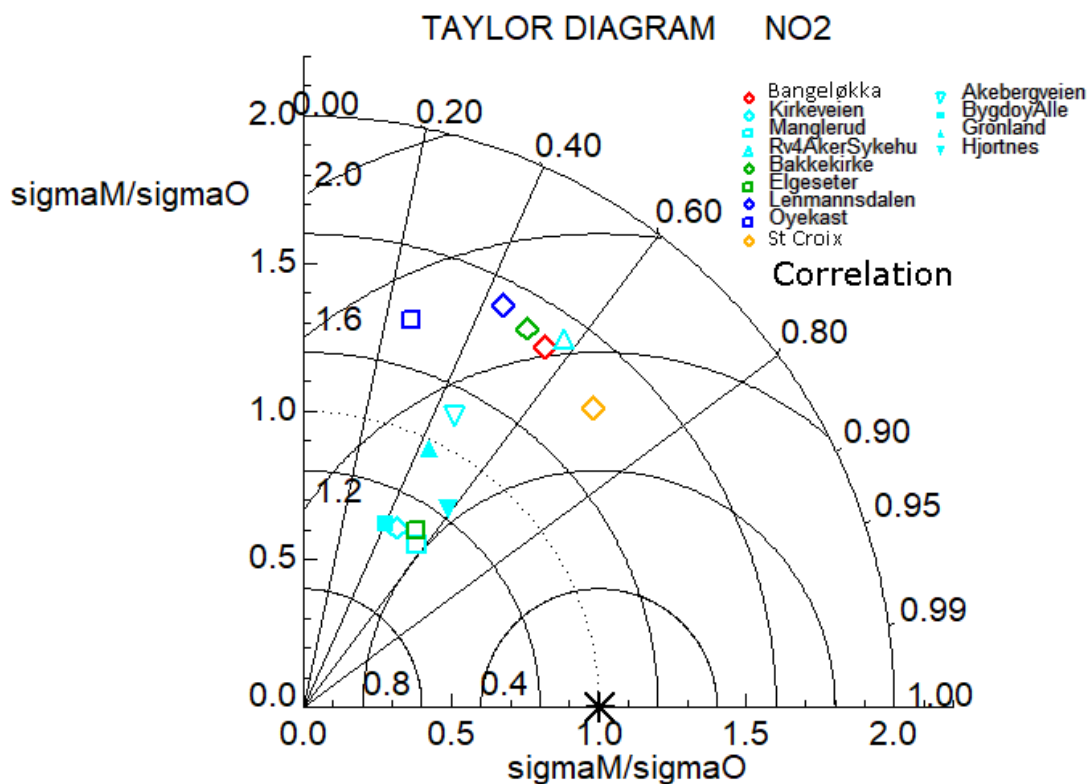
Figure 10. A Taylor diagram calculated using the summer only (June, July, and August) hourly time series of NO₂ concentrations for thirteen in-situ stations used for the model evaluation across five out of the six domains (excluding Stavanger). The symbols are colour coded according to each model domain where Drammen is red, Oslo is cyan, Trondheim is green, Stavanger is pink, Grenland is dark blue, and Nedre Glomma is orange. The x and y-axis both represent the ratio of the model standard deviation to the observed standard deviation in NO₂ concentrations for a particular station, such that points can be plotted on concentric circles centred on the x/y origin. The correlation is plotted according to the azimuthal angle from the origin represented as a series of straight lines emanating from the x/y origin. Lastly, the RMSE (units µg m⁻³) is also represented for each station according to their linear distance from 1.0 on the x-axis.
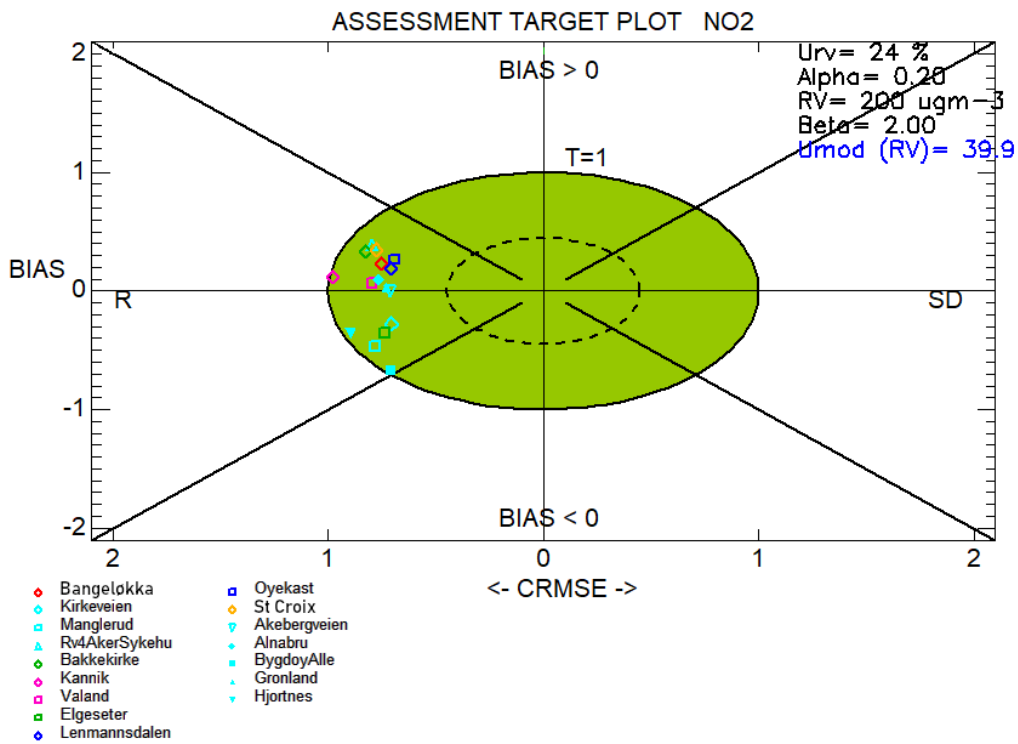
Figure 11. Target plots created with hourly time series of NO₂ concentrations for 2015 for all sixteen in-situ stations used for the model evaluation across all six domains. The symbols are colour coded according to each model domain where Drammen is red, Oslo is cyan, Trondheim is green, Stavanger is pink, Grenland is dark blue, and Nedre Glomma is orange.

Figure 12. Target plots created using the winter only (December, January, and February) hourly time series of NO₂ concentrations for all sixteen in-situ stations used for the model evaluation across all six domains. The symbols are colour coded according to each model domain where Drammen is red, Oslo is cyan, Trondheim is green, Stavanger is pink, Grenland is dark blue, and Nedre Glomma is orange.
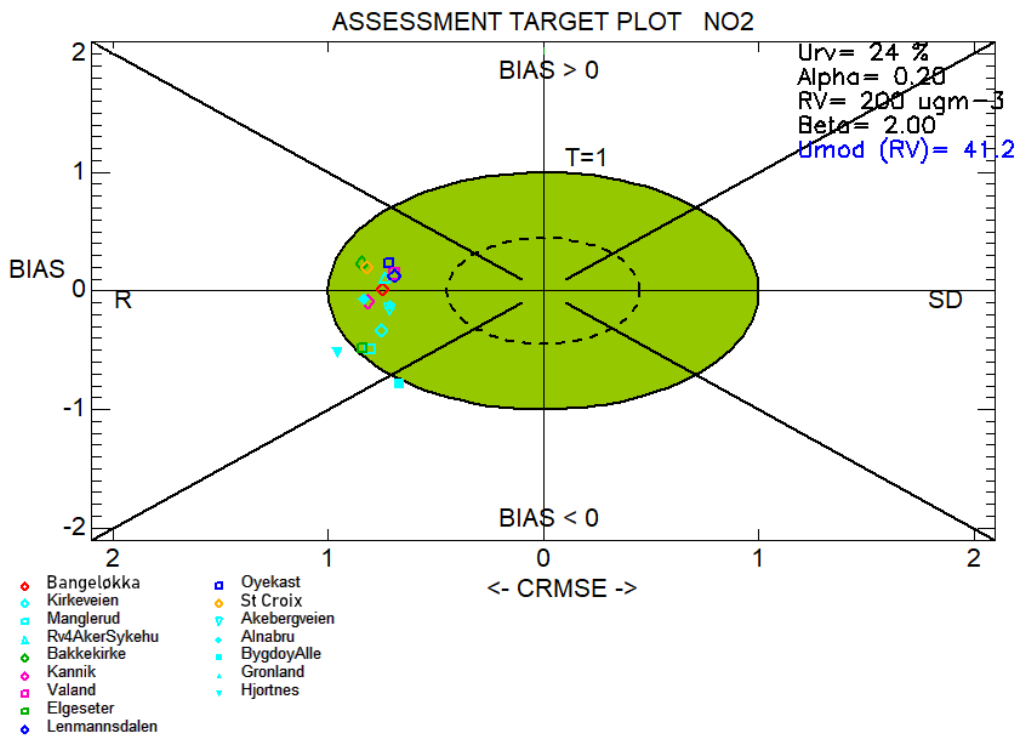
Figure 13. Target plots created using the summer only (June, July, and August) hourly time series of NO₂ concentrations for thirteen in-situ stations used for the model evaluation across five out of the six domains (excluding Stavanger). The symbols are colour coded according to each model domain where Drammen is red, Oslo is cyan, Trondheim is green, Stavanger is pink, Grenl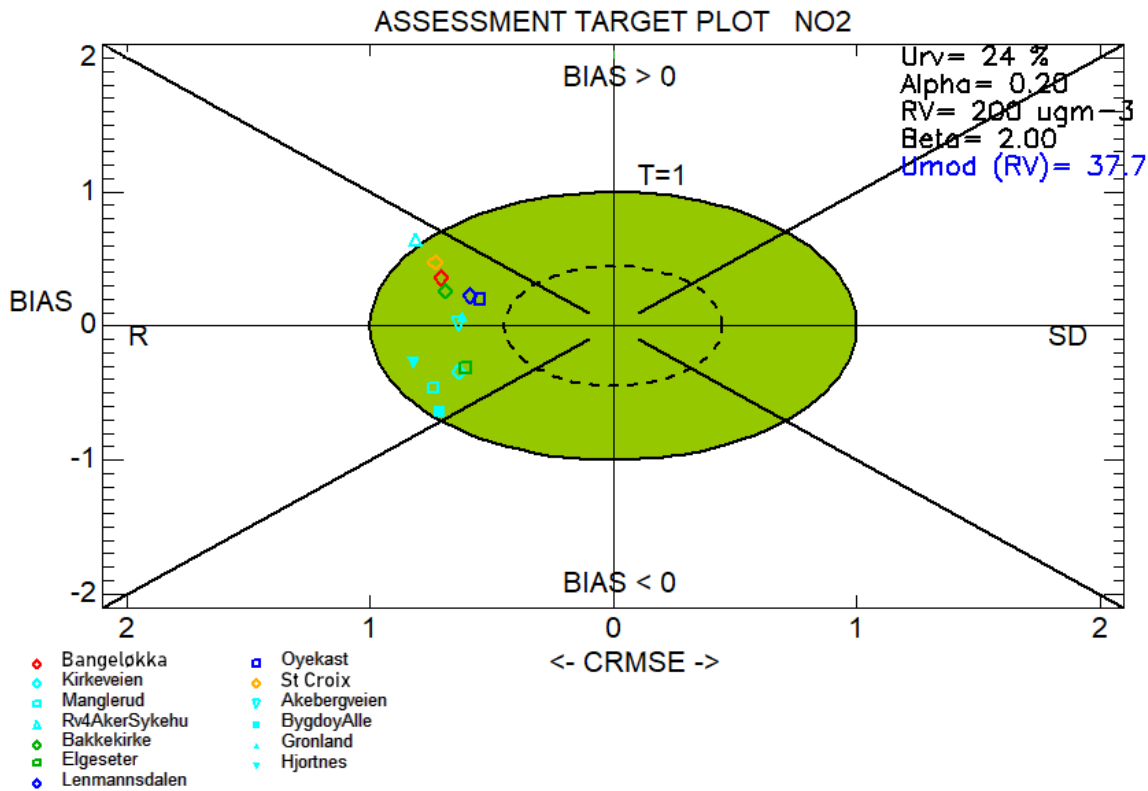and is dark blue, and Nedre Glomma is orange. Note that there are 3 missing stations (Rv4 Aker Sykehus, Kannik, and Våland) during the summer analysis due to insufficient data.
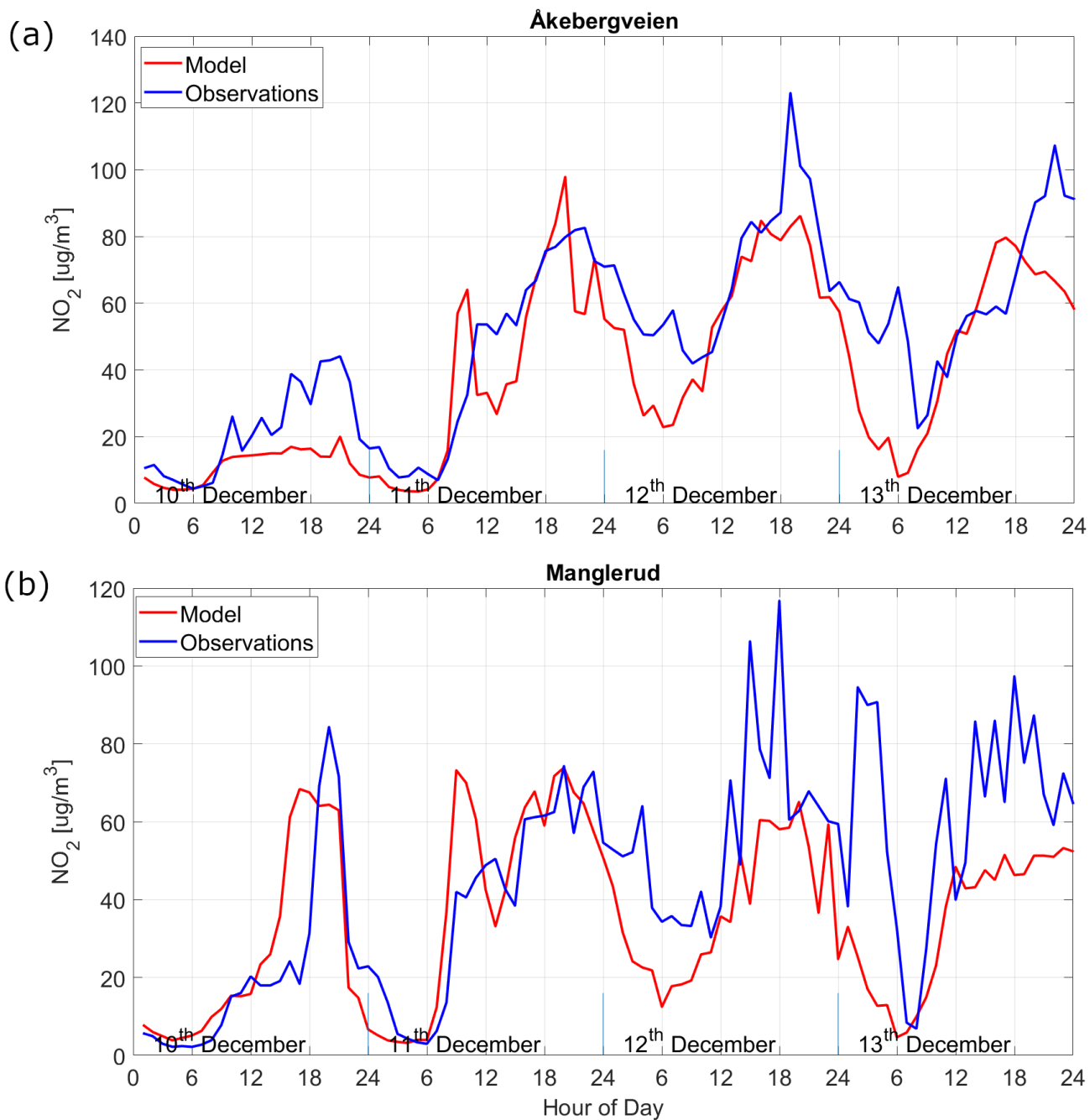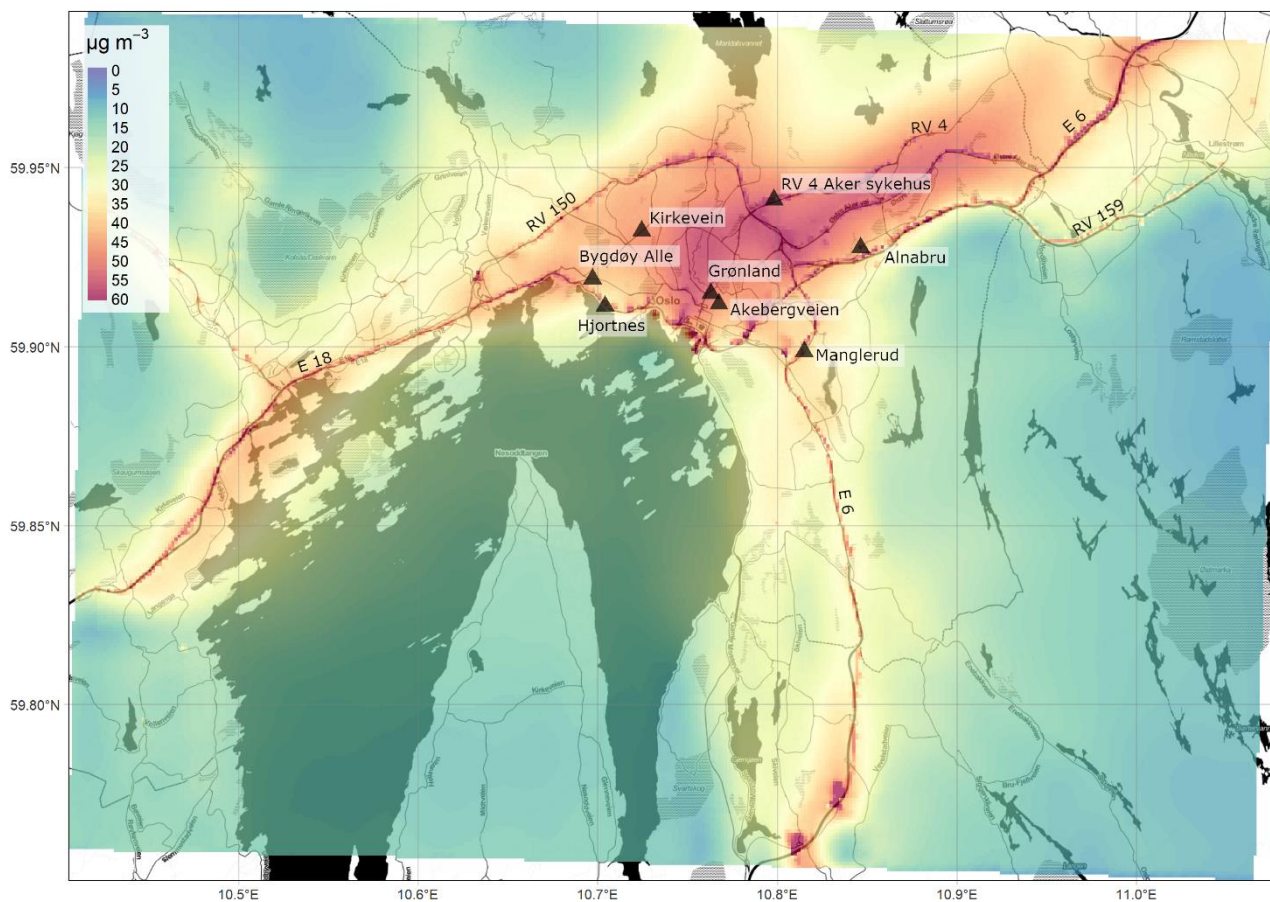
Figure 14. Time series of NO₂ concentrations for the (a) Åkebergveien and (b) Manglerud measuring station in Oslo during a pollution episode lasting from December 10th to 13th 2015. Receptor point concentrations from the model are shown in red, and the observed concentrations are shown in blue.

5

Figure 15. Simulated daily mean NO$_2$ concentrations for December 11th from the EPISODE model over the Oslo domain at 100 m x 100 m spatial resolution. This day was selected from a pollution episode lasting from December 9th until December 13th. The concentrations are derived from the receptor point concentrations and then re-gridded onto a 100 m grid. The colour scale shows the range in annual mean NO$_2$ concentrations between 0 and 60 µg m^{-3}. The black triangles indicate the locations of the air quality observation stations (Table 7). The dark shaded areas represent the sea, lakes and rivers. The black lines are roads. © OpenStreetMap contributors 2019. Distributed under a Creative Commons BY-SA License.
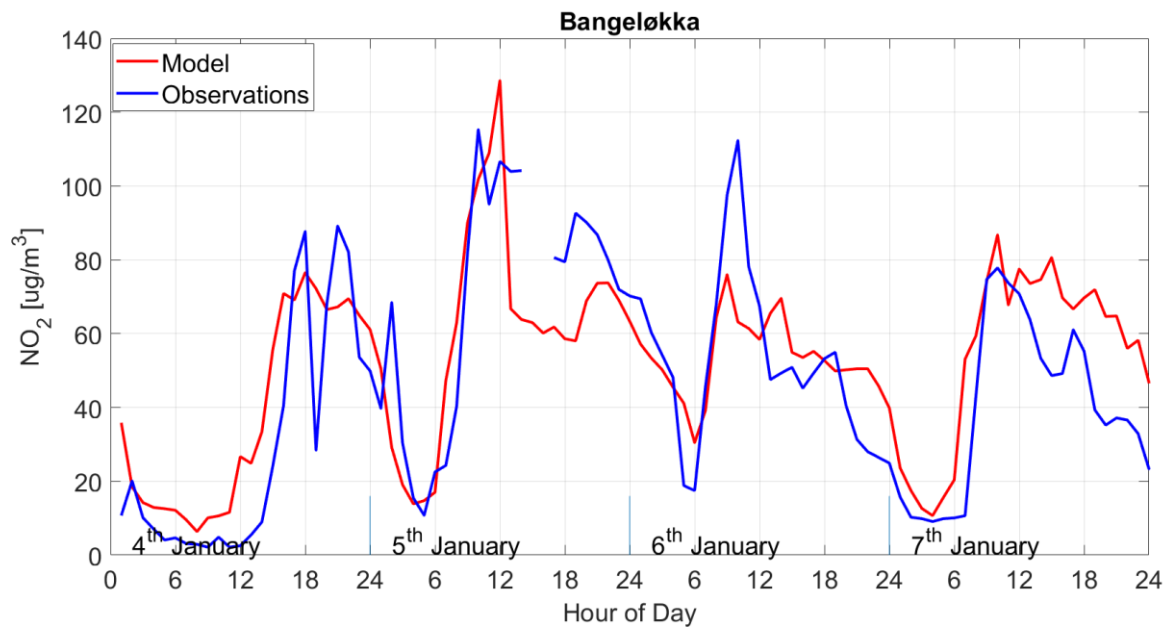
Figure 16. Time series of NO$_2$ concentrations for the Bangeløkka measuring station in Drammen during a pollution episode lasting from January 4th to 7th 2015. Receptor point concentrations from the model are shown in red, and the observed concentrations are shown in blue.
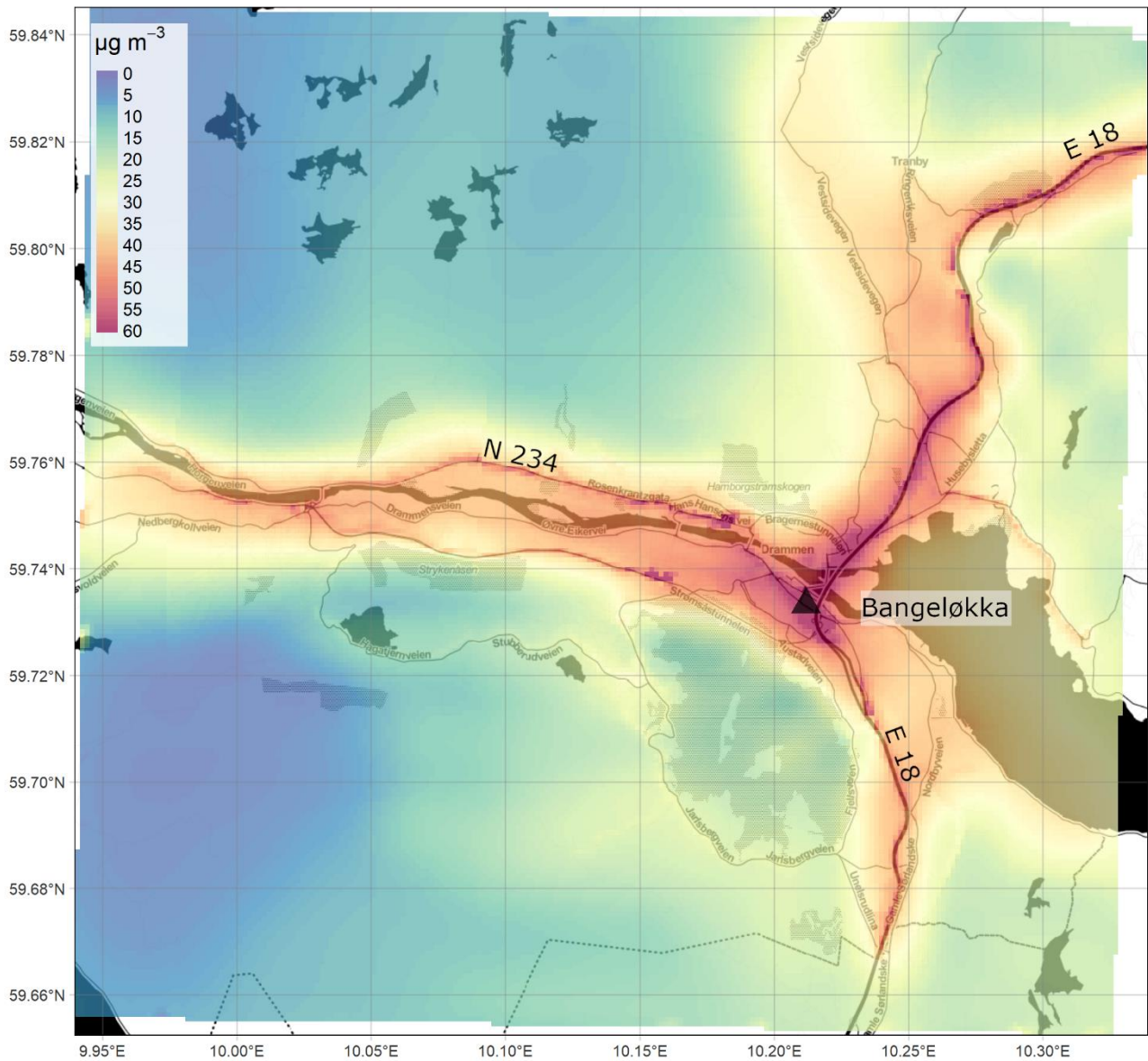
Figure 17. Simulated daily mean NO₂ concentrations for January 5th from the EPISODE model over the Drammen domain at 100 m x 100 m spatial resolution. This day was selected from a pollution episode lasting from January 4th until January 7th. The concentrations are derived from the receptor point concentrations and then re-gridded onto a 100 m grid. The colour scale shows the range in annual mean NO₂ concentrations between 0 and 60 µg m⁻³. The black triangles indicate the locations of the air quality observation stations (Table 7). The dark shaded areas represent the sea, lakes and rivers. The black lines are roads. © OpenStreetMap contributors 2019. Distributed under a Creative Commons BY-SA License.

Table 1. A compilation of all of the possible 3D advection and diffusion schemes usable for the EPISODE Eulerian grid transport.

Process	Options	Usage	Description/reference
Horizontal advection	Positive definite 4th degree Bott scheme	Recommended for use in EPISODE	Bott (1989, 1992, 1993)
	Positive definite and monotone 4th degree Bott scheme	Experimental, for test purposes only	Bott (1992, 1993)
Advection in the vertical	Simple upstream method	Recommended for use in EPISODE	Byun et al. (1999)
Horizontal diffusion	Fully explicit forward Euler scheme.	Recommended for use in EPISODE	(Smith, 1985)
Vertical diffusion	Semi-implicit Crank-Nicholson diffusion scheme	Recommended for use in EPISODE	Byun et al. (1999)
	Urban K(z) method	Newly implemented method, and recommended for specific applications	Beljaars and Holtslag (1991)

Table 2. A list and description of all of the possible methods to include initial and background pollutant concentrations in EPISODE model simulations.

Method	Temporal Specification	Data Format
Constant concentration over the entire domain	Constant in time	Set in input runfile
Constant concentration over the entire domain evolving in time	Hourly	ASCII file
Identical concentration column profile covering the entire domain in each vertical layer	Constant or hourly	ASCII file
3D concentration field	Hourly	ASCII file or NetCDF file

Table 3. Description of the pre-processing utilities used for preparing input files for the EPISODE model.

Pre-processing Utility	Purpose	Required Input	Pre-processing Output
MCWIND	MCWIND creates diagnostically fields of meteorological variables using meteorological observations	Meteorological observations (temperature, wind speed, relative humidity, wind direction, precipitation, and cloud cover) from two or more meteorological observation stations. Requires the observed differential in temperature between two heights in order to infer vertical stability.	Meteorological fields on the EPISODE model horizontal and vertical gridding. All variables can be specified in ASCII or binary format. MCWIND can also create constant topography and surface roughness fields across the entire domain.
CAMSBC	Downloads and interpolates the CAMS regional air quality forecasts to the EPISODE modelling domain and grid	Downloaded CAMS regional forecast in NetCDF or GRIB2 formats	Interpolated initial and background concentrations for the EPISODE model domain
UECT	UECT produces the various emission input files for point sources, line sources and area source categories independently of AirQUIS	Emission data of geo-referenced or gridded yearly emission totals for NO_x, NMVOC, CO, SO2, NH3, PM2.5 and PM10 in a tabular CSV file	Emission input files in ASCII-format for EPISODE containing hourly varying emission data defined for each source category and pollutant
TAPM4CC	TAPM4CC creates 2-D and 3-D meteorological fields based on output from the TAPM model	TAPM *.outa file of a simulation with the number of vertical layers matching that of the EPISODE model domain	Hourly meteorological 2-D and 3-D (24 vertical layers up to 3750 m height) and topography input files in binary format for use in EPISODE
Auxiliary utilities	Utilities for creating topography and surface roughness input files for EPISODE.	One can either extract the topography and surface roughness from the WRF and AROME meteorological files, or you can specify constant values across the domain	Input files of surface roughness and topography in ASCII format for the EPISODE model domain (only relevant when running with AROME meteorology)

Table 4. A description of the data sources, the methodology used, and the reference years for the emission inventories for each emission sector used in the case studies. NRA: Norwegian Road Administration, OFV: Opplysningsrådet for Veitrafikken. HBEFA: Handbook Emission Factors for Road Transport. NCA: Norwegian Coastal Administration. NPRTR: Norwegian Pollutant Release and Transfer Registers.

Emission Sector	Data Source	Methodology	Reference Year
On road	NRA (ADT), HBEFA (EF), OFV (Vehicle fleet technology composition)	Traffic emission model	2013
Off road	Statistics Norway	Statistics at the district level and gridding using GIS software	Drammen (2012), Oslo (1995), Stavanger (1998), Trondheim (2005)
Shipping	NCA, except in Oslo, for which it was used data provided by the Port of Oslo and NILU databases described in López-Aparicio et al., 2017	AIS and Activity data (Oslo)	2013
Industrial	Statistics Norway, facility level and NPRTR	Emission officially reported by entities or estimated based on data from facilities	Drammen (2012), Grenland (1991/2015), Nedre Glomma (2012), Oslo (2013), Stavanger (1998/2015), Trondheim (2005/2015)

5

Table 5. A description of the emission type and the percentage emission of NO$_x$ as NO$_2$ (as NO2 mass equivalent) for each sector considered in the model simulation case studies.

Emission Sector	Emission Type	Percentage emission of NO$_x$ as NO$_2$ in terms of NO$_2$ mass equivalent
On road	Line source	Varying between 4.5% to 45.9% (with an approximate mean of 15%)
Off road	Area source	10%
Shipping	Area source	10%
Industrial	Area source (point sources in Grenland)	10%

5 **Table 6. A description of the horizontal extent, vertical gridding (shown as the height at the top and at the mid-level of each layer) with the mid-level points shown in brackets) and the number of receptor points for each model domain. Note that identical vertical gridding was used for all six cities.**

Model domain	Horizontal extent (km × km)	Vertical gridding – Layer tops (m)	Vertical gridding – mid-layer heights (m)	Number of receptor points
Oslo	38 × 27	24, 48, 72, 98, 125, 153, 184, 218, 254, 294, 338, 386, 436, 493, 552, 621, 692, 771, 858, 950, 1050, 1157, 1275, 1401, 1538, 1686, 1844, 2016, 2195, 2387, 2591, 2805, 3032, 3270, 3518	12, 36, 60, 85, 111.5, 139, 168.5, 201, 236, 274, 316, 362, 411, 464.5, 522.5, 586.5, 656.5, 731.5, 814.5, 904, 1000, 1103.5, 1216, 1338, 1469.5, 1612, 1765, 1930, 2105.5, 2291, 2489, 2698, 2918.5, 3151, 3394	34040
Trondheim	14 × 16	idem	idem	10293
Stavanger	14 × 25	idem	idem	16496
Drammen	23 × 22	idem	idem	13758
Grenland	16 × 23	idem	idem	13661
Nedre Glomma	29 × 22	idem	idem	28498

Table 7. Observation stations used in the evaluation of the EPISODE model results for the six different city domains. The location of each station is shown in UTM coordinates along with the corresponding UTM grid.

City/Domain	Observation Station	UTM Coordinates (X-UTM,Y-UTM)		Station Type
Oslo	Åkebergveien	598845,	6642929	Traffic
	Alnabru	603212,	6644794	Traffic
	Bygdøy Alle	594854,	6643637	Traffic
	Gronland	598697,	6642974	Urban background
	Hjortnes	595188,	6642860	Traffic (high volume)
	Kirkeveien	596377,	6645131	Traffic (high volume)
	Manglerud	601533,	6641533	Traffic (high volume)
	Rv4 Aker Sykehus	600444,	6646186	Traffic (high volume)
Drammen	Bangeløkka	568124,	6622332	Traffic (low volume)
Nedre Glomma	St Croix	611082,	6565092	Traffic (high volume)
Grenland	Lensmannsdalen	193449,	6570117	Traffic (high volume)
	Øyekast	193541,	6566749	Influence from industry and harbour
Stavanger	Kannik	311922,	6540558	Traffic (high volume)
	Våland	311898,	6540686	Urban background
Trondheim	Bakke Kirke	570411,	7034630	Traffic
	Elgeseter	569691,	7033059	Traffic (high volume)

5

10

Table 8. Mean statistics presented in the Taylor for all sixteen observation stations for the full year, the winter, autumn, and summer seasons. σM/σO is the ratio of the model and observed standard deviation in NO$_2$ concentrations, R is the Pearson correlation coefficient, RMSE is the Root-mean squared error (units µg m^{-3}), and IOA is the index of agreement. These statistical metrics are explained in further detail in Appendix C.

Time Period	σM/σO	R	RMSE	IOA
Annual	1.05	0.6	0.95	0.74
Winter	0.90	0.64	0.84	0.76
Autumn	1.16	0.62	0.98	0.74
Summer	1.11	0.5	1.09	0.65

5

Table 9. Compiled statistics for the comparison between the observed and modelled NO$_2$ concentrations during the December 10th to 13th pollution episode in Oslo. Statistics for each station are shown along with the mean of all of the statistics. σM/σO is the ratio of the model and observed standard deviation in NO$_2$ concentrations, R is the Pearson correlation coefficient, RMSE is the Root-mean squared error (units µg m^{-3}), and IOA is the index of agreement. These statistical metrics are explained in further detail in Appendix C.

10

Station	σM/σO	R	RMSE	IOA
Alnabru	0.58	0.57	0.82	0.66
Manglerud	0.79	0.61	0.81	0.75
Rv4 Aker Sykhus	0.94	0.65	0.81	0.80
Bygdøy Alle	0.66	0.74	0.68	0.67
Kirkeveien	0.85	0.75	0.67	0.78
Gronland	0.81	0.77	0.64	0.83
Åkebergveien	0.97	0.84	0.56	0.88
Hjortnes	0.52	0.84	0.63	0.73
Mean	0.77	0.72	0.70	0.76